MAGMA SPEEDOMETRY: DETERMINING THE KINETICS

OF THE HORNBLENDE BREAKDOWN REACTION

A SINIOR THESIS SUBMITTED TO

THE DEPARTMENT OF GEOLOGY AND GEOPHYSICS

UNIVERSITY OF HAWAI'I AT MĀNOA

AUGUST 2007

By

Lisa Tatsumi

Thesis Advisor

Julia Hammer

ABSTRACT

Mount St. Helens Wn dacitic pumice erupted 1480 y.b.p. was used for high temperature laboratory decompression experiments to study the formation of rims on hornblende crystals in response to magma decompression. The sample is evolved magma with 67.2 wt.% bulk SiO_2, and is also highly crystalline with glass SiO_2 of 74.8 %. It last equilibrated at ~850 °C and $X_{H_2O}^{fluid} = 0.25$-0.30 at 350 MPa according to a previous study (Gardner et al., 1995). Three sets of time-series experiments using temperature as the independent variable allow us to quantify the temperature dependence of the reaction rate and investigate the rate law governing hornblende breakdown. All runs were brought to 850 °C and 130 MPa, and held for 24 hours. They were decompressed to 65 MPa and held at either 810, 850, or 890 °C for variable durations. Measured rim widths for each sample were used to generate plot of rim width vs. square root of time and Avrami (ln-ln) plots. Constants k and n, a reaction rate constant and a constant dependent on mechanism, were obtained from the regression lines of the plots and used to generate best fit curves for the rim width or completion fraction vs. time. The results show a significant temperature control on reaction rate. Also, distinct values of n for 850 and 890 °C indicate non-isokinetic nature of the reaction, which suggests temperature dependency of rate limiting steps in the hornblende breakdown reaction.

INTRODUCTION

Hornblende breakdown reaction

Hornblende is a hydrous mineral that is abundant in arc magmas. Volcanoes formed at converging plate boundaries typically have magma with relatively high water content. This is due to water in the downgoing oceanic plate, which is released during subduction and causes the overlying mantle to partially melt. The water-rich melts rise through the mantle and continental plate, gather in crustal magma chambers, and finally erupt at arc volcanoes. As the magma ascends to the Earth's surface during an eruption, dissolved water becomes gaseous and escapes due to lowering of pressure. Because hornblende has OH-group in its structure, the mineral becomes unstable under dehydrating conditions attained during the ascent of magma. If the eruption rate is moderate, allowing sufficient time for the magma to at least partially equilibrate chemically, hornblende starts to dissolve into the liquid. Anhydrous minerals such as clinopyroxene, orthopyroxene, plagioclase, and Fe oxides crystallize to form a reaction rim around the original hornblende crystal. Consumption of components from both the hornblende and the matrix melt form the reaction rim products (Buckley et al., 2006). A partially reacted hornblende crystal within a lava dome rock erupted from Mount St. Helens in 1982 is shown in Figures 1 and 2. In this case, the presence of an unreacted core indicates that the reaction did not go to completion during the magma's ascent to the surface.

Magma ascent rate determination

It is important to understand the hornblende breakdown reaction because it allows us to estimate magma ascent rate from the widths of hornblende reaction rims using the following equation:

$$magma\_ascent\_rate\left[\frac{m}{s}\right] = depth\_of\_chamber[m] * \frac{rim\_advance\_rate\left[\frac{mm}{s}\right]}{measured\_rim\_width[mm]}$$

(Eq. 1)

in which the depth of chamber must be known independently. The equation shows it is possible to calculate the rate of magma ascent by measuring the thickness of the reaction rim of hornblende if the rate of rim advance is known (Rutherford and Gardner, 2000). Although this equation is simplification because the rate of rim advance is not necessarily constant with time, the hornblende reaction may provide an approximate "magma speedometer". Magma ascent rate is very difficult to obtain using geophysical methods or other chemical techniques.

A pioneering experimental study was conducted by Rutherford and Hill (1993) on Mount St. Helens May 18, 1980, dacite. Magma ascent rates were determined from amphibole reaction rims using the experimental calibration of rim width versus time. Subsequently, these results have been used to interpret eruptions of other magmas and other volcanoes including 1995-2002 Soufriere Hills in Montserrat (Rutherford and Devine, 2003). However, the method is strictly only applicable to the specific conditions of the experimental study; that is, 1980-1986 Mount St. Helens dacite at 900 °C at H_2O saturation, 1995-2002 Soufriere Hills andesite at 830-860 °C at H_2O saturation (etc.). Moreover, even for Mount St. Helens magmas, the rate law, mechanism, and effect of temperature are not understood well. Other studies indicate that several variables control the rate of formation of reaction rim on hornblende, notably, magma composition, temperature, pressure and amount of dissolved water (Rutherford and Hill, 1993; Garcia and Jacobson, 1979; Rutherford and Gardner, 2000). Extending the hornblende magma speedometer to other situations requires that we study the reaction in the laboratory to isolate these variables. An understanding of the kinetics will

3

enable a general application of the method.

Selection of Wn as starting material

Mount St. Helens 1480 y.b.p. Wn dacite pumice was selected as starting material. It was chosen for several reasons. First, Mount St. Helens is an important volcano to study from a hazards perspective. It is presently the most active volcano in the cascades arc, and has produced effusive and large explosive eruptions within the past 30 years. Also, the phase equilibria of the Wn pumice were studied well by Rutherford (1985). Secondly, the temperature should be high enough for the reaction to proceed on a laboratory time scale. From ilmenite-magnetite pairs, the last equilibrated temperature of the Wn magma was determined to be 850 °C by Gardner et al. (1995), which is likely to be high enough to have ideal rim advance rate. Using the solubility calculator of Moore (1995), it was determined that the Wn magma attains water saturation at 130 MPa and 850 °C with 4.8 wt.% H_2O. One important constraint is the pressure-temperature limitation of the experimental apparatus. The vessel that we use for high temperature and pressure experiments cannot withstand elevated pressure (200 MPa) at temperatures greater than 900 °C. Therefore, Wn pumice sample satisfied the temperature and pressure requirements, and was suitable for achieving further understanding on Mount St. Helens magma.

Temperature as an experimental parameter

In this study, we focused on temperature as an experimental variable because it is expected that its control over the reaction rate is the greatest (Putnis, 1992). The exponential increase with the temperature increase for most chemical reactions shows that they are thermally activated. If an Arrhenius plot (ln(reaction rate constant) vs. 1/(temperature) $[K^{-1}]$) using data obtained in the experiment provides a line, it will allow me to find the activation

4

energy of rim growth from its slope. This will enable interpolation of the reaction rates for any temperature within the range spanned by the experiments.

The pre-eruptive temperature of Wn pumice, approximately 850°C, was used as the initial temperature of all experiments. Final temperature after single decompression was varied either 810, 850, or 890 °C. The high and low temperatures are reasonable maximum and minimum eruption temperatures for dacite magma. Also, taking the vessel strength into consideration, 890°C was selected to be the highest final temperature. Therefore, the difference between the middle temperature and the other two temperatures is 40°C, and the lowest temperature was set to 810 °C. To a first approximation, the reaction rate inferred from the rim advance against time for these three temperatures is mainly a function of temperature. At P_{H_2O} of 65 MPa and temperature of 810 and 850 °C, hornblende is similarly unstable in this magma, as estimated from the inferred shape of the hornblende stability curve (Figure 3). At 890 °C, the run conditions are further "below" the hornblende curve, and therefore suggest a larger thermodynamic driving force for the breakdown reaction.

Kinetics of the hornblende breakdown reaction

Bamford and Tipper (1980) describe three characteristic kinetic behaviors of solid state chemical reactions: acceleratory, sigmoidal, and deceleratory. Acceleratory behavior is described by a power law or exponential function, in which the reaction rate progressively increases. This is obviously not sustainable throughout the irreversible reaction because the reactants are eventually consumed. The most common deceleratory behavior is described by parabolic function, and it is due to diffusion control on the reaction (Figure 4 a). Such behavior exists if reaction products form at the interface between reactants and create a barrier layer that grows with time. Sigmoidal behavior involves both features, described by

5

Avrami-Erofe'ev equation. It takes into account elimination of a site when volume is consumed by a growing nuclei, and coalescence, or overlap of unreacted volume where two growing nuclei meet (Figure 4 b).

Considering solid state reactions, diffusion is commonly a significant rate limiting step compared to nucleation and growth (Bamford and Tipper, 1980). Moreover, if the hornblende reaction rim serves as a barrier layer impeding access of melt to the hornblende surface, diffusive control may be large. Thus, the hornblende breakdown reaction is tentatively expected to follow the parabolic function. However, it is not certain how much other rate limiting steps contribute to the reaction. Therefore, Avrami-Erofe'ev rate law should also be considered because it takes account nucleation and growth rates as well as diffusion rate. Hence, it is expected that either the parabolic rate law or Avrami-Erofe'ev rate law explains the hornblende breakdown reaction, which should be tested.

Parabolic rate law

The hornblende breakdown reaction rate may follow a deceleratory rate equation, in which the completion fraction of the reaction is proportional to square root of time (Bamford and Tipper, 1980). The model was suggested based on the experiment on epidote reaction rim growth in granitic magma by Brandon et al. (1996). Epidote is only stable at high pressure in granitic magmas. The existence of epidote in granitic rocks in shallower crust infers the rapid rate of upward transportation of magma. Thus, the epidote breakdown reaction also may be used to estimate the magma ascent rate from the reaction rim width similarly to hornblende. A plot of epidote reaction rim width versus time is a parabolic curve, indicating that the reaction rate is proportional to square root of time. The parabolic nature of the reaction progress through time is interpreted to indicate diffusion rate as the rate-

6

limiting step. Although it has been carried out by using epidote not hornblende, the basic kinetics is likely to be similar for both minerals due to the similarity in their reaction types. However, only three data points are included in the epidote study. This limits the strength of interpretation of reaction mechanism, as well as the confidence with which rates may be interpolated between experimental temperatures.

Avrami-Erofe'ev rate law

The rate may follow a sigmoid rate equation (Bamford and Tipper, 1980), one of which is the Avrami equation

$$y = 1 - \exp(-(kt)^n) \qquad \text{(Eq. 2)}$$

where y is completion fraction of the reaction, k is a rate constant, t is time, and n is a constant depends on the mechanism for isothermal kinetics. This equation is the general form of empirical rate equation for heterogeneous reactions involving several phases (Putnis, 1992). According to Avrami theory, a plot of fraction transformed, equivalent to rim width normalized by maximum rim width, vs. time yields a curve close to S-shape. The rate of reaction gradually increases at the beginning until it attains constant rate (acceleratory stage) and decreases when all liquid turns into solid state (deceleratory stage) (Bamford and Tipper, 1980). This type of rate behavior was observed in hornblende breakdown experiments by Rutherford and Hill (1993). They also observed a lag time before a measurable rim forms while the concept of lag time is not a part of the Avrami theory.

METHODS

Starting material preparation

Original sample

The sample SH-591-1 Wn Dacitic pumice from 1480 y.b.p. eruption was kindly

collected by Siggurdson, Carey, and Gardner, and provided by Rutherford. Comparing its chemical composition with other arc magmas of Redoubt (1989), Mount St. Helens (1980), Unzen (1991-1995), and Soufriere Hill (1995-1997), Wn magma is the most evolved with 67.2 wt.% bulk SiO_2, and is also highly crystalline with glass SiO2 of 74.8 % (Table 1). Analyses of 10 ilmenite-magnetite pairs in Wn dacite, and application of the Anderson and Lindsley oxide geothermometer reveal that the sample last equilibrated at 850 °C and oxygen fugacity of $10^{-12.12}$ bars (equivalent to 0.8 log units above Ni-NiO buffer curve). Phase equilibria experiments and mineral/glass compositions of this dacite suggest that $X_{H_2O}^{fluid} =$ 0.25-0.30 at 350 MPa. However, experimental glass compositions also closely match the natural glass at $X_{H_2O}^{fluid} = 0.4$-0.5 at 250 MPa and $X_{H_2O}^{fluid} = 0.8$-0.9 at 150 MPa (Gardner et al., 1995). For technical reasons, including relative ease of capsule preparation, we chose to run experiments at H_2O-saturation ($X_{H_2O}^{fluid} = 1.00$). The magma is H_2O-saturated with ~4.80 wt.% H_2O at 130 MPa. Hence, the conditions for a 24 hours anneal period, which ensures that the pumice is restored to magma pre-eruptive conditions, are 850 °C and 130 MPa. This value is lower than higher limit of pressure that vessels can resist. As a post-eruptive pressure, 65 MPa was selected at which reacted hornblende crystals showed the maximum rim advance rate in the experiments on dacite pumice by Gardner (1995). It allowed us to minimize the limitation of the number of experimental runs due to time constraints.

Hornblende Concentrate

SH-591-1 Wn pumice contains only 1.5 volume % hornblende (Gardner et al., 1995). Therefore, hornblende crystals were extracted from part of the pumice to combine with original pumice to create a starting material with at least 10 wt.% hornblende. This step ensures that each change contain enough hornblende crystals for robust analysis, yet not so

8

many that the bulk composition or breakdown reaction is significantly affected.

The majority of the pumice clast is white and unoxidized. However, there was a small dark gray anomalous portion that may be a mingled component. It was removed with a chisel to ensure that the starting material has a uniform composition. The sample was first crushed with a hammer to sub-cm size grains. The sample was crushed further with a plattner mortar and pestle, and then with a ceramic mortar and pestle to less than 1 mm.

The crushed material was sorted with a stack of 8 cm diameter cylindrical metal sieves with mesh size of 0.991 mm, 0.495 mm, 0.250 mm, and 0.124 mm. The 0.124 mm sieve was selected as a smallest mesh because the grains were to undergo magnetic mineral separation, in which grain size of approximately 0.100 mm is a lower practical limit. First, dry sieves cleaned with an ultra sonic water bath were stacked together with the bottom pan. Some of the crushed sample was poured into the top sieve of the sieve stack with the coarsest mesh. The stack of the sieves with the top lid closed was shaken horizontally by hand for about one minute. Then, it was rested for several tens of seconds waiting for small particles to settle down. The sorted grains were separated into vials. In order to make certain that all of sample go through at least the top sieve, the grains left in the coarsest sieve with 0.991 mm mesh were put into the mortar and ground. The procedure was repeated until all the samples were fall into one of four size ranges: <0.124 mm, 0.124-0.250 mm, 0.250-0.495 mm, and 0.495-0.991 mm. The weight proportions of the resultant splits for each size were 34.8%, 13.5 %, 22.5 %, and 29.2 % from small size to large size.

The splits with size range 0.124 mm -0.250 mm were eventually selected to undergo magnetic separation of hornblende crystals based on photomicroscopic observation on the grains of all sizes and some trials using the magnetic separator. This range of grain size

consists of glasses and individual hornblende crystals, which provides higher possibility to separate hornblende crystals from glass or other minerals through magnetic separation. Before the sample underwent a magnetic mineral separation, a standard hand magnet was used to remove magnetite. The magnetite-poor splits were run through the magnetic mineral separator (Frantz Isodynamic Separator Model L-1). A schematic drawing of the equipment is shown in Figure 5. The slope angle of the separator perpendicular to the direction of sample path (labeled as A) was set to 20°, and the slope angle parallel to the direction of sample path (labeled as B) was set to 30°. The magnetic field was set to 0.8 A taking a published value of the hornblende magnetic susceptibility into consideration (Hess, 1966). Vibration strength was set to the maximum value, 10. The grains without magnetite were poured into the feed hopper on the top of the slide little by little to prevent clogging. The magnetic fraction contained mostly hornblende, with a minor amount of pyroxene and Fe oxides is called "hornblende concentrate".

Starting material for each capsule

Grains from all 4 splits including removed magnetite were recombined to produce 2 g of starting material containing the original, intrinsic concentration of hornblende. (The 0.250-0.495 mm split from which hornblende was removed to produce hornblende concentrate was not included.) Hornblende concentrate was mixed with this powder when each experimental charge was made, in the mass proportions 1:9, respectively.

Experimental Methods

Experimental charges

Four mm outer diameter Ag or $Ag_{70}Pd_{30}$ alloy tubes were used to make capsules in which samples were sealed. These materials were used because they isolate the sample from

the pressurizing medium (water), have melting points higher than the experimental run temperatures (961.93 °C and 1170 °C, respectively), and react minimally with the sample. The tubes were cut into approximately 25 mm lengths (slightly longer for Ag, due to its difficulty in welding) using a steel blade. The inner walls of the tubes were cleaned with kimwipe soaked with ethanol. One end of the tubes was crimped and closed with rounded needle-nose pliers. The closed end was welded with an oxy-acetylene torch. Approximately 10 wt.% (~0.01 g) of distilled water was added to each capsule using a syringe to attain water saturated condition inside charges throughout experiments. Approximately 0.072 g hornblende depleted original powder was mixed with 10 wt.% hornblende concentrate (~0.008 g) to produce approximately 0.08 g total powder for each charge, except for SHW-01 and SHW-04 with the total solid mass of 0.1 g as a trial. The mixed powder was carefully added to the capsule. The top of the capsule was crimped with pliers just above the silicate powder to confine powder and water in a relatively limited region inside the capsule, and welded. The weld joint was checked under an optical microscope and charge was put into a 50 °C oven for at least 20 minutes. The weight of subsequently cooled capsule was compared to the weight recorded before heating to detect a decrease of mass corresponding to water loss through pinholes in the weld joints. After assuring successful welding, charges were named SHW-(number) and stored in individual envelopes on which information such as mass of solid, final water mass, and final water wt.% was recorded.

Assembly

A schematic drawing of the furnace assembly is shown in Figure 6. Ni alloy pressure vessel and Ni filler rods were used for the experiments. Water was used as the pressurization medium. Pressure was recorded with a pressure transducer checked against a factory-

11

calibrated Heise gauge and were considered accurate to 0.5 MPa. An iron gland nut assembly was used to connect the 1 1/4" O.D. (outer diameter) vessel to the 1/16" O.D. tubing to the 1/4" O.D. pressure line. A K-type thermocouple was used to monitor temperature at a location close to the sample at the hot end of the vessel.

Single-step decompression experiments

A total of 25 experiments were conducted, including failures and replicate runs (Table 2 and Figure 7). The failure rate was 12 %. The failures of experiments were due to clogging of flexible tubing of the connector, loss of pressure inside the vessel, power interruption, and thermocouple failure. First, experimental runs were maintained at the initial conditions 850 °C and 130 MPa for 24 hours. After 24 hours at the initial condition, the pressure was immediately lowered to 65 MPa and the temperature was changed to the final temperature, either 810, 850, or 890 °C.

Run procedure

A charge was slid into the Ni alloy pressure vessel so that the bottom of the charge goes to the end of the vessel. Ni filler rods prevent convection and help ensure uniform sample temperature throughout the run. The vessel was connected to the pressure line by iron gland nut assembly and water was induced from the line by opening the valve at the line-assembly connection. A pressure check was conducted before putting the vessel into the furnace, in order to assure that there was no water leaking from the vessel. First, the water line was isolated from the water reservoir by closing the reservoir valve in order to detect small change in pressure. The line pressure was raised to a high value such as 200 MPa, and then closing the vessel valve. In 1-1.5 hours, the pressure inside the vessel was checked by adjusting line pressure to the expected vessel pressure, opening the vessel valve, and closing

it again after several seconds. Any drop more than 0.5 MPa was attributed to water leaking, and was considered unacceptable. Connections were tightened until there was no drop in pressure. The reservoir valve was opened and line pressure was set to 105 MPa. Anticipating an increase in pressure due to heating of water inside the vessel, this value was sufficient to produce the desired anneal pressure of 130 MPa. Temperature of the furnace is set to the initial condition, 850 °C prior to starting the experiment because it takes for a while for the furnace to achieve the target temperature. The vessel was put into the furnace, and simultaneously, a sheathed K-type thermocouple was inserted into the ~2 cm deep hole at end of the vessel close to the charge located inside. Temperature and pressure were recorded every 5 minutes for approximately 20 minutes to make certain it was operating well. Within roughly 20 minutes, the sample achieved the initial temperature and pressure in the line stopped increasing rapidly. Pressure was adjusted if it did not reach or exceeded the target pressure. The vessel valve at the line-vessel was kept open for 1.5 hours and closed at the target pressure to buffer small increases in pressure as the vessel thermally equilibrated.

The temperature and pressure were maintained at the initial condition for 24 hours, then decompressed to the final condition. First, the reservoir valve was opened. Temperature and pressure were set to the desired final condition, and the vessel valve was opened. The pressure was set slightly lower than the target value for the higher final temperature (890 °C), in anticipation of the expecting increase in pressure due to increase in water temperature. After temperature and pressure were stabilized, the vessel valve was closed.

The sample was quenched after pre-determined duration at final conditions. First, the reservoir and vessel valves were opened with line pressure at the final condition. Then, the furnace lid was opened. The vessel was lifted and removed from the furnace, and it was

13

cooled with compressed air until it no longer glowed red. The air-cooled vessel was plunged into a bucket of water for further cooling. The quench rate experienced by the sample is on the order of minutes.

Taking out charges from vessels

The charges were taken out from the disconnected vessels and briefly checked for breakage under a photographic microscope. A small cut was made on the charges away from the location where rock sample is located by cutting pliers, and the charges were left in the oven at 50 °C for at least 20 minutes. The charges were taken out from the oven, and rock sample inside the charges were taken out by peeling the capsule off using pliers. Sample chips were put into small glass vials, including any small particles, and labeled.

Analytical methods - image processing

Making thin sections

Very fine particles were used to make grain mounts before making thin sections. The particles were put on a glass slide, and a cover slip was put on the top. Several drops of an index of refraction liquids (n = 1.600 ± 0.0002) were placed close to the edge of the cover slip, which were let be sucked beneath the cover slip by capillary action. The grain mounts were observed using a petrographic microscope and initial observation of hornblende crystals were made.

The largest resultant rock samples were chosen to make thin sections. The pieces of rocks were mounted in 2-part Hillquist (A + B) epoxy, and the surface to be attached to the glass slides was abraded flat and smoothed with 400 and 1200 alumina grits by hand on a thick glass plate. The rocks with solidified epoxy were attached to frosted glass slides with the same epoxy. In this step, quartz grains were also poured on the epoxy seeped out around

14

the rock sample, as a helpful aid in checking the thickness of the section. The decreasing interference colors in the quartz grains signaled decreasing section thickness. After the epoxy solidified, the extra rock sample on the slide was sliced off with a diamond wafering blade using a high speed saw with rotation speed 650-750 rpm, and stored as a spare. The surface of the thin sections was abraded with 400 and 1200 alumina grits by hand. Using a Buehler slide holder and a lapping wheel rotating 100-300 rpm, samples were polished with 9 and 6 μm Diamat, and 0.1 μm alumina slurries.

Obtaining reflected light images

Olympus BX51 Pol Scope petrographic microscope and Olympus C5050 Zoom 5 megapixel digital camera were used to obtain reflected light images of thin sections. They were similar to the back scattered electron images. These images were used to locate hornblende crystals within samples, and as maps to guide the locations of hornblende in scanning electron microscope. Either 2x or 4x was used for the objective lens magnification depending on the size of the sample. If the sample did not fit in the view, parts of the sample were taken separately and combined later with Adobe Photoshop to obtain the images of the whole samples.

Obtaining back scattered electron (BSE) images

The thin sections were coated with approximately 25 nm thick carbon with a carbon coater. The edges of the thin sections covered by carbon tape, and polished islands were connected with strips of carbon tape to provide an efficient pathway for electrical conduction in the scanning electron microscope (SEM). BSE images of all recognized hornblende crystals in thin sections were obtained using a JEOL JSM 5900LV SEM. Three thin sections at maximum were put into the SEM at the same time. BSE images were saved as TIFF

15

images with magnification and scale bar on the lower left.

Measuring rim width

Rim width was measured for at least 10 crystals for each experimental run except for 3 crystals for SHW-23 that has less than 10 crystals suitable for rim width measurement. BSE images were opened in the image analysis program ImageJ. A scale bar embedded in the image by SEM was used to set true scale in ImageJ. 10 μm x 10 μm white grid points were overlaid on the images and the points closest to the hornblende perimeter were painted pink. Lines were drawn from the hornblende perimeter to the outer perimeter of the furthest rim phase, intersecting the pink dots and perpendicular to the tangents of the hornblende perimeters. The length of the lines was automatically calculated using the command "measure". Grids make it possible to measure rim width approximately every 10 μm. An example image under the process is shown in Figure 8. A strength of method is that it provides an objective basis for selecting sites for rim width measurement. It was deemed reproducible by conducting replicate analyses. A possible weakness is comparability with results from other studies, which employ different methods.

The rim width of each sample was taken as the mean of the all measurements on crystals for each sample. This was a plausible assumption because thickness value distribution followed the normal distribution (e.g., Figure 9). It was confirmed based on the normalized cumulative frequency vs. rim width plots and quantile plots for samples SHW-06, 11, 12, and 15-2 (Figure 10).

Normal distribution plausibility confirmation - normal distribution and normal quantile plots

The mean, minimum, maximum, and standard deviation of all measurements on 3-16 crystals for each sample (typically several hundred measurements per sample) were

16

determined using Microsoft Excel. The thicknesses of each rim were classified into one of

10 bins whose intervals were determined by (max - min)/10. The frequencies of thicknesses

in 10 bins for each crystal were normalized so that mean rim width is not biased by sizes of

hornblende crystals. These values were combined to produce the frequency distribution of all

measurements. The final distributions were plotted as normalized cumulative frequency vs.

rim width. The normal distribution curve was generated using the probability density

function

$$f(x) = \frac{1}{\sigma\sqrt{2\pi}} \exp\left(-\frac{(x-\mu)^2}{2\sigma^2}\right) \qquad \text{(Eq. 3)}$$

where μ and σ are the population mean and the population standard deviation for all crystals

within one sample, respectively. The bins, or rim thickness range, same as the plot

mentioned above were used. The obtained frequency for each bin was normalized and

plotted in the same graph (Kirkup, 2002; e.g., Figure 9). This method rather visually

provides an approximate confirmation of normal distribution of the data.

As another confirmation, normal quantile plots were generated by following the steps

described by Kirkup (2002). The quantile plot of the experimental data should be linear if

the distribution is normal. First, experimental data x_i were ordered from smallest to largest,

where i is the arbitrary number assigned to each datum. Secondly, the fraction of values f_i

that were less than or equal to the ith value were calculated using the relationship

$$f_i = \frac{i - \frac{3}{8}}{n + \frac{1}{4}} \qquad \text{(Eq. 4)}$$

where n is the total number of values in the sample. Third, quantile, $q(f_i)$ was calculated for

all the fractions, f_i ($i = 1, 2, \ldots, n$), for the standard normal distribution using

17

$$q(f_i) = 4.91 \left[f_i^{0.14} - (1 - f_i)^{0.14} \right] \qquad \text{(Eq. 5)}$$

Finally, a graph of x_i vs. $q(f_i)$ was generated. The resultant distribution of data plots was approximately linear except for those with small rim widths (<5 μm). The coefficients of determination of the plot were small (0.9886, 0.9599, 0.9543, and 0.9867). Therefore, the normal quantile plots confirmed a normal distribution of the rim width measurements.

RESULTS

Rim crystal texture

Several BSE images of quenched samples are shown in Figure 11. A summary of the texture of hornblende and rim crystals based on BSE image observation is shown in Table 3. Rim crystals are pyroxene, plagioclase, and Fe-Ti oxides. Roundness of hornblende crystal becomes greater as time at final temperature increases. The morphologies of rim crystals are subhedral and vary from equant to elongated within each experimental run. This is presumably due to a non-random crystallographic orientation of each crystal in the thin sections. The hornblende crystals that are elongated (probably roughly parallel to c axis) in the images typically have elongated rim crystals. This is especially prominent for pyroxene; hornblende in near-basal section has rim crystals that are more equant. Rim crystals are sparsely distributed around hornblende crystals for shorter time at final conditions while relatively packed for runs with longer duration. This dispersive characteristic was seen in both radial and tangential directions. The size range of rim pyroxene crystals showing equant shape was estimated by taking average size of 5 smallest and 5 largest crystals on one hornblende crystal that has larger amount of such rim pyroxene crystals compared to others. The shortest diameter of rim crystals in the images was measured to keep consistency. Also,

it is assumed to be less variable compared to the longest diameter considering cutting angle of pyroxene. The range for all runs was 0.5-14.4 μm. In general, the maximum size increases with time except for drop in value for SHW-08 for 890 °C. Hornblende crystals for the longest duration at 890 °C, showed very small remnant hornblende crystals and large rim width. There were some clusters of crystals that were considered as rim phases of reacted hornblende crystals, where the original hornblende cores appeared not to be present. The observation may imply that the original hornblende crystals were completely reacted. On the other hand, its appearance may be due to the way reacted hornblende was exposed to the surface of the thin sections. For example, if its exposure to the surface of the thin section was only a part of a very thick rim, it appears to be no remaining hornblende core even if the hornblende was actually still present. If the apparent disappearance of hornblende cores of the reacted crystals for this run was the actual complete consumption of original hornblende crystals due to the reaction, the presence of such crystals suggests that some of the reactions within the run had proceeded until all the original hornblende crystal was consumed.

Some features such as roundness of hornblende crystals and dispersion of rim crystals seem to vary with experimental duration (Table 3). Also, they seem to depend on temperature based on the image comparisons among the experimental runs shown with the same superscriptions in Table 3 (e.g., SHW-04, 09, and 12 at 210.1-215.1 hours). However, the morphology of rim crystals including size is consistent for all three temperatures, suggesting that the reaction occurs at the same mechanism in all temperatures. However, other data such as aspect ratios, proportions, and chemical composition of different rim phases should be considered before concluding that the reaction stoichiometry or mechanism remains constant over this temperature range.

Rim width

The average and standard deviation of the rim width for each crystal are listed in Table 4. The thickness values for individual crystals were combined as described above to yield a characteristic thickness representing each experimental run. The values were used to produce rim width vs. time, and extent of reaction completion vs. time plots (Figure 12). Error bars were obtained from the equation $\frac{\sigma}{\sqrt{n}}$, where σ is standard deviation of all rim width measurements and n is the number of measurements within each run. This error assessment represents accuracy of the measurements rather than the spread of the data about the mean.

At 810 °C, the rim width seemed to increase with time. However, at the longest duration (SHW-18 with 1982.2 hours), no rim growth was observed and the hornblende crystals showed relatively sharp edges (not rounded). It is difficult to physically interpret the results. One possible human error involved in this run is that the thermocouple was not inserted to the vessel correctly. The automatic heating of the furnace to achieve the target temperature values is based on the detection of temperature by the thermocouple. In this case, the furnace is heated excessively to reach the target value, resulting in the higher temperature that the sample is exposed to than it ought to. However, at higher temperature, it is expected show larger rim width, therefore, this possible human error is unlikely to contribute to a lack of rim on the hornblende crystals in the sample. Hence, the reason for the unexpected result remains to be uncertain. At 850 °C, the rim width nearly consistently increased with time. The thickest rim was 19.56 µm for 975.2 hours (SHW-15-2), which was similar rim width as the most of runs for 890 °C. It is desired to have an experimental run in longer duration to see if hornblende crystals attain larger rim width, for instance, the assumed maximum rim

20

width 30 μm. At 890 °C, the rim width increases with time overall. However, the transition from no-rim to with-rim was abrupt, resolved by the experiments at $\leq$ 12 hours. Also, the rim widths do not consistently increase between 24.1 and 215.6 hours. In fact, the data are quite noisy in this time range. More experiments with the durations between the transition zones are desired.

Parabolic plot

A plot of rim width (μm) vs. square root of time (hours) is shown in Figure 13. The completion fraction, y, can be calculated and used for this plot similarly to the plot for the parabolic rate law shown in Figure 4 a, assuming 30 μm was a maximum rim width achieved at completion of the breakdown reaction based on our experimental results of rim growth. However, the completion of the reaction and its timing are not taken into consideration in the process of generating parabolic fits. Therefore, the raw rim width instead of completion fraction was used to generate parabolic plots. For those runs that showed no rim, only the results for the longest duration were included in the graph. The data points for each temperature were shifted toward negative x direction by square root of time of the first zero rim data points. The linear regressions of the plots were obtained using Microsoft Excel with zero Y-intercept. The coefficients of determination for linear regressions for this plot were not significantly close to 1.0 for the cooler temperatures (0.79, 0.80 for 810, 850 °C) and very poor (-0.03) for 890 °C.

The plot of rim width (μm) vs. time (hours) with parabolic fits is shown in Figure 14. For each temperature, the values of slopes for linear regressions obtained in the plot in Figure 13 were substituted for the equation

$$y = (slope) * t^{1/2} \qquad \text{(Eq. 6)}$$

The rim width values for corresponding time with an increment of 5 hours were determined by inputting t into Eq. 6, and were plotted against time to produce parabolic fits.

Avrami Plot

The empirically found isothermal kinetics of a wide range of mineral reactions can be described by the equation

$$\frac{dy}{dt} = k^n t^{n-1}(1-y) \qquad \text{(Eq. 7)}$$

where y is completion fraction of rim growth obtained assuming 30 μm as the maximum rim width, t is the time at final conditions, n is a constant that depends on mechanism of the reaction, and k is rate constant. However, k in this equation is not the same sense as seen in more general rate equation

$$\frac{dy}{dt} = k.f(y) \qquad \text{(Eq. 8)}$$

By integrating the function and combining $1/n$ into the constant k, the Avrami equation (Eq. 2) was obtained. It was further rearranged into the form of

$$-\ln(\ln(1-y)) = n \ln(k) + n \ln(t) \qquad \text{(Eq. 9)}$$

A plot generated using this linearized equation is called the Avrami plot, where $-\ln(\ln(1-y))$ is plotted against $\ln(t)$. From the slope and Y-intercept of this plot, the values of n and k can be determined. The values are substituted back into Eq. 2, and it is used to generate a sigmoidal curve in y vs. t plot.

The Avrami plot for our experiment is shown in Figure 15. The data points with zero rim width were omitted because they cannot be plotted on a ln scale. Those for 115.6 and 362.3 hours at 850 °C (SHW-01 and 15) were replaced with replicate runs (SHW-20 and 21) because the latter are more internally consistent with adjacent experiment rim width results.

22

Error values were obtained by calculating difference between $-\ln(\ln(1-y))$ and $-\ln(\ln(1-(y \pm$

$\frac{\sigma}{\sqrt{n}}$)). The linear regressions were generated using Microsoft Excel. Because there were

only two data points for 810 °C, the Avrami parameters for this temperature are not

overdetermined, as for the other temperatures. The constant n, dependant on the reaction

mechanism was determined to be 1.75 for 850 °C and 0.65 for 890 °C from the slope of the

linear regressions for the Avrami plot. The constant k was calculated by inputting n into

exp((Y-intercept)/n). It turned out to be 0.0010 for 850 °C and 0.0091 for 890 °C. The

coefficients of determination for linear regressions for the Avrami plot were 0.89 and 0.69

for these temperatures.

Curves of y vs. t were generated using Avrami equation (Eq. 2) with n and k values

obtained from Avrami plot (Figure 16). The point for 1982.2 hours at 890 °C (SHW-18) was

disregarded in this plot in addition to two replaced experiments mentioned above because the

absence of the reaction rim in this sample is clearly inconsistent with the theory. The curves

for all temperature appeared to fit relatively well except for the one for 890 °C, in which

points for the intermediate durations seem to have unclear trend. Nonetheless, the coefficient

of determination for this temperature is better in Avrami plot (Figure 15) than in parabolic fit

(Figure 13).

Comparisons and summary of plots

Because the coefficients of determination for the parabolic rate law and those for the

Avrami plot were similarly good, and the regression lines for the lowest temperature for both

plots were not reliable (only 2 and 3 data points, respectively), comparison on the

coefficients of determination cannot be used to determine which rate law is more likely to

23

describe to the hornblende breakdown reaction. Therefore, it is difficult to decide which fit is better.

The parabolic rate law regression line and fit appears to be good fits. However, strict interpretation of the parabolic rate law does not include the notion of lag time, or delay in reaction onset, at the beginning of the reaction. Unlike a deceleratory law such as the Avrami-Erofe'ev rate law, a diffusion controlled process is fastest at short times. Therefore, in this aspect, the Avrami-Erofe'ev rate law may be considered as more reasonable rate law to explain the reaction. On the other hand, the process of rim development may follow diffusion control if we allow for a lag time during which diffusion is not the rate-limiting step.

Distinct n values for 850 and 890 °C for the Avrami plot indicate that the mechanism is not isokinetic across the temperature range between 850 and 890 °C. Ideally, we would have more data points for the lowest temperature to investigate the temperature dependence of n.

Arrhenius plot

Using constant k from the Avrami plots, an Arrhenius plot is constructed to examine the nature of the temperature dependence of the reaction rate constant ($\ln(k)$ vs. $1/$(temperature) [K^{-1}]; Figure 17). The plot shows the temperature dependence of the reaction rate explicitly having temperature as a variable of its one of axes, unlike any other plots generated in this study. A coherent trend on this plot would facilitate interpolation of reaction rates for intermediate temperatures. If the alignment of the three points in the Arrhenius plot were linear, it would suggest that the reaction is isokinetic, that is, having the same mechanism across the tested temperature range. If the plot is linear, it is also possible to determine the activation energy, E_a, of the reaction from the slope of the Arrhenius plot

regression that is equivalent to $-E_a/R$, where R is a gas constant (8.3145 [J/kg K]).

Because the constant k determined from the Avrami plot for 810 °C is not reliable due to insufficient number of data points in Avrami plot, the value for this temperature in the Arrhenius plot is tentative or speculative. Thus, a true linearity of the Arrhenius plot cannot be determined. However, based on the fact that the n values for the Avrami plot for 850 and 890 °C were distinct that suggests non-isokinetic nature of the reaction, the Arrhenius plot is unlikely to be linear in the temperature range between 850 and 890 °C. Again, it is necessary to have more data points for the lowest temperature to substantiate this hypothesis. Also, data points at intermediate temperatures in the Arrhenius plot would be helpful to deduce the true nature of the Arrhenius plot.

The two rate laws and other possibilities

In this project, it turned out that it was difficult to determine which of the rate laws represent the hornblende breakdown reaction better, the Avrami-Erofe'ev rate law or the parabolic rate law, based on the plots due to lack of enough experimental data points. However, some characteristics features that are related to the kinetic behaviors were identified: presence of lag time and deceleratory rate progress with increasing time.

The sluggish initial rate of rim formation exemplified by 5 experiments in which no rims were observed may represent time required for dissolution of hornblende into the surrounding liquid, and structural organization of the liquid, prior to nucleation and growth of rim phases. In that case, it might be better to take the induction time into consideration for two rate laws that does not involve it in their theories.

A deceleratory feature of the fit curves is consistent with the apparent flattening of rim thickness at longer durations in the experimental run results from our study and those of

Rutherford and Hill (1993) and Browne and Gardner (2006). On the other hand, the flattening is not universally observed in the natural samples represented by completely reacted hornblende crystals in the magmas from arc volcanoes (e.g., Mount St. Helens, Mount Merapi, etc.). This suggests the flattening, or the parabolic feature of the rim growth vs. time might be an artifact. This discrepancy might be due to difference in experimental and natural conditions such as volatile constituents and composition of the gas phase, size of hornblende crystals, rate of decompression, and thermal history, which should be also paid attention in the future studies.

In comparison to natural samples, the reaction rim crystals were sparse. It suggests that there is no barrier layer that slows down transport of reactants to the hornblende surface, as expected. Therefore, the reaction may not necessarily follow the parabolic rate law. Instead, it is possible that it follows the sigmoid rate equation such as the Avrami-Erofe'ev equation. However, to continue this study, it is crucial to analyze the interstitial melt within rims and in the groundmass in order to determine whether there is a chemical gradient, that is, a boundary layer in melt composition rather than crystalline reaction products that would suggest diffusion control.

It is also possible that there are better methods for fitting model. Wang et al. (2004) introduced refined Avrami method to generate their models for the exsolution of pentlandite from the monosulfide solid solution. In this method, it was assumed that the activation energy of the reaction is a function of reaction extent. Therefore, according to the authors, the new method provides more detailed variation of kinetic parameters throughout the reaction. Although the reaction used for their study is distinct from hornblende reaction in some aspects including mechanisms and experimental temperature and time ranges, this idea

26

suggests possibility of better fit using a refined conventional method.

CONCLUSIONS

Findings

The clearest result is the extreme temperature dependence of the hornblende breakdown reaction. A plot of rim width vs. time clearly indicates that higher temperature leads to faster rim growth. Behavior of the fit curves is distinct for all temperatures regardless of which rate equations were used to create them. For 890 °C, there is no discernible lag time, meaning that it must be ≤ 12 hours, if it exits. The onset of rim formation is progressively delayed as temperature is reduced. Therefore, it is important to know the precise control of temperature on reaction rim formation in order to improve the applicability of hornblende reaction rim measurements as a magma speedometer.

Secondly, rate limiting step for the reaction may vary for different temperatures. Distinct values of n for Avrami plots for different temperatures (850 and 890 °C) indicate reactions for each temperature has different reaction mechanism, in other words, the reaction is non-isokinetic.

Although the rate law that the hornblende breakdown reaction follows could not be determined from the data and plots obtained in this study, the results provided some important insights to the kinetic behavior of the reaction. The general statement by Bamford and Tipper (1980) that solid-liquid chemical reactions are likely to be governed by the diffusion rate seem to match with our resultant rim width vs. time curves with deceleratory behavior at longer duration. Also, presence of lag time along with deceleratory feature suggests a possible necessity of introducing the notion of induction time to the rate law.

27

Future work

Referring to the findings, more data points with intermediate durations for each temperature are desired. Also, it is ideal to have a few additional series of data for intermediate temperatures. These data will allow us to understand precise temperature control on the reaction because it can be conducted by attempting to obtain the best fits to the data points similarly to in this study, in which the outcome is better with more data points. Similarly, additional data points will help gain additional values of n for comparison and give more confidence to the hypothesis that the hornblende breakdown reaction is not isokinetic or may change the hypothesis. The additional data points are also likely to lead to better fits, which will give us more precise kinetic behavior.

Despite well-developed theoretical predictions of kinetics, the mechanism of the reaction may be inaccessible, considering the uncertainties and variance in our data set. However, it is important to constrain the nature of the temperature control over the rate by fitting the data using a model that produces the lowest misfit, and determine the temperature dependence of the fit parameters. As for models, it may be necessary to suggest new modeling methods or implement refinements to of the conventional model based on theories, as conducted by Wang et al. (2004).

Limits of application to other volcanic samples

The plot of rim width vs. time serves as a calibration that can be applied to the determination of magma ascent rates. Given a rim width, the time that magma took to arrive at the surface after its breakdown reaction started in the magma chamber can be estimated. The ascent rate is calculated by dividing the depth of chamber at which the breakdown reaction began by the duration time spent below magma camber pressure. Therefore, as long

28

as the calibration is dependent on its experimental conditions and sample's chemical compositions, the magma ascent rates for only those samples experienced the identical conditions can be determined using the calibration. Therefore, it seems highly difficult to achieve a general application of hornblende magma speedometer. However, if the reaction is isokinetic throughout a certain temperature range, and the Arrhenius plot is obtained, and also if the sample's last equilibrated temperature is known, it is possible to interpolate the plot and determine rate constant for any intermediate temperature, in which hornblende reaction rim can be considered as slightly more applicable. In order to understand the kinetics of the reaction better, it is important to continue this study.

REFERENCES

Bamford, C. H. and Tipper, C. F. H. (ed), *Comprehensive chemical kinetics: 22 reactions in the solid state*, Elsevier Scientific Publishing Company, Amsterdam, 1980.

Brandon, A. D., Creaser, R. A., and Chacko, T., Constraints on rates of granitic magma transport form epidote dissolution kinetics, *Science*, **271**, 1845-1848, 1996.

Browne, B. L. and Gardner, J. E., The influence of magma ascent path on the texture, mineralogy, and formation of hornblende reaction rims, *Earth and Planetary Science Letters*, **246**, 161-176, 2006.

Buckley, V. J. E., Sparks, R. S. J., and Wood, B. J., Hornblende dehydration reactions during magma ascent at Soufriere Hills Volcano, Montserrat, *Contributions to Mineralogy & Petrology* **151**, 121-140, 2006.

Garcia, M. O. and Jacobson, S. S., Crystal clots, amphibole reaction and the evolution of calc-alkaline magmas, *Contributions to Mineralogy & Petrology* **69**, 319-327, 1979.

Gardner, J. E., Rutherford, M. J., Carey, S., and Sigurdsson, H., Experimental constraints on pre-eruptive water contents and changing magma storage prior to explosive eruptions of Mount St Helens volcano, *Bulletin of Volcanology*, **57**, 1-17, 1995.

Hess, H. H., Notes on operation of Frantz Isodynamic Magnetic Separator: *SG Frantz Co. Instrument Instruction Booklet*. 1966.

Kirkup, L., *Data analysis with Excel: an introduction for physical scientists*, Cambridge University Press, 2002.

Moore, G., Vennemann, T., and Carmichael, I. S. E., Solubility of water in magmas to 2 kbar, *Geology (Boulder)*, **23**, no.12, 1099-1102, 1995.

Putnis, A., *Introduction to mineral sciences*. Cambridge: Cambridge University Press, 1992.

Rutherford, M. J., The May 18, 1980, eruption of Mount St. Helens, 1. melt composition and experimental phase equilibria, *Journal of Geophysical Research*, **90**, 2929-2947, 1985.

Rutherford, M. J., Magma ascent rates from amphibole breakdown: an experimental study applied to the 1980-1986 Mount St. Helens eruptions, *Journal of Geophysical Research*, **98**, 19667-19685, 1993.

Rutherford, M. J. and Devine, J. D., The May 18, 1980, eruption of Mount St. Helens, 3. stability and chemistry of amphibole in the magma chamber, *Journal of Geophysical Research*, **93**, 11949-11959, 1988.

Rutherford, M. J. and Gardner, J. E., Rates of magma ascent, *Encyclopedia of Volcanoes*, 2000.

Wang, H., Pring, A., Hgothai, Y., and O'Neill, B., A low-temperature kinetic study of the exsolution of pentlandite from the monosulfide solid solution using a refined Avrami method, *Geochimica et Cosmochimica Acta*, **69**, 415-425, 2005.
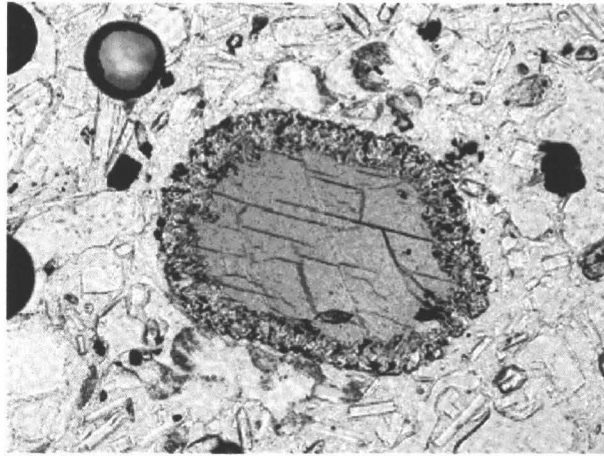
Figure 1 Optical photomicrograph of a sample of the 1981 dome of Mount St. Helens (provided by JE Hammer). The brown crystal at center is hornblende. Rim of smaller transparent and opaque crystals are minerals formed by breakdown reaction occurring due to reduced H_2O content of surrounding melt. This is the same crystal as the one shown below with a scale.
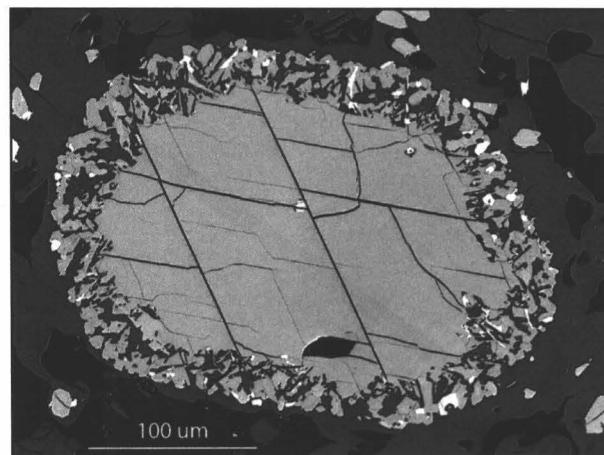

Figure 2 Back-scattered electron micrograph obtained using a scanning electron microscope of the same hornblende crystal as Figure 1. The gray scale values of this image reflect the mean atomic number (Z) of the sample: bright crystals are rich in iron (large Z), light gray crystals are pyroxenes, dark gray crystals are feldspars (small Z).
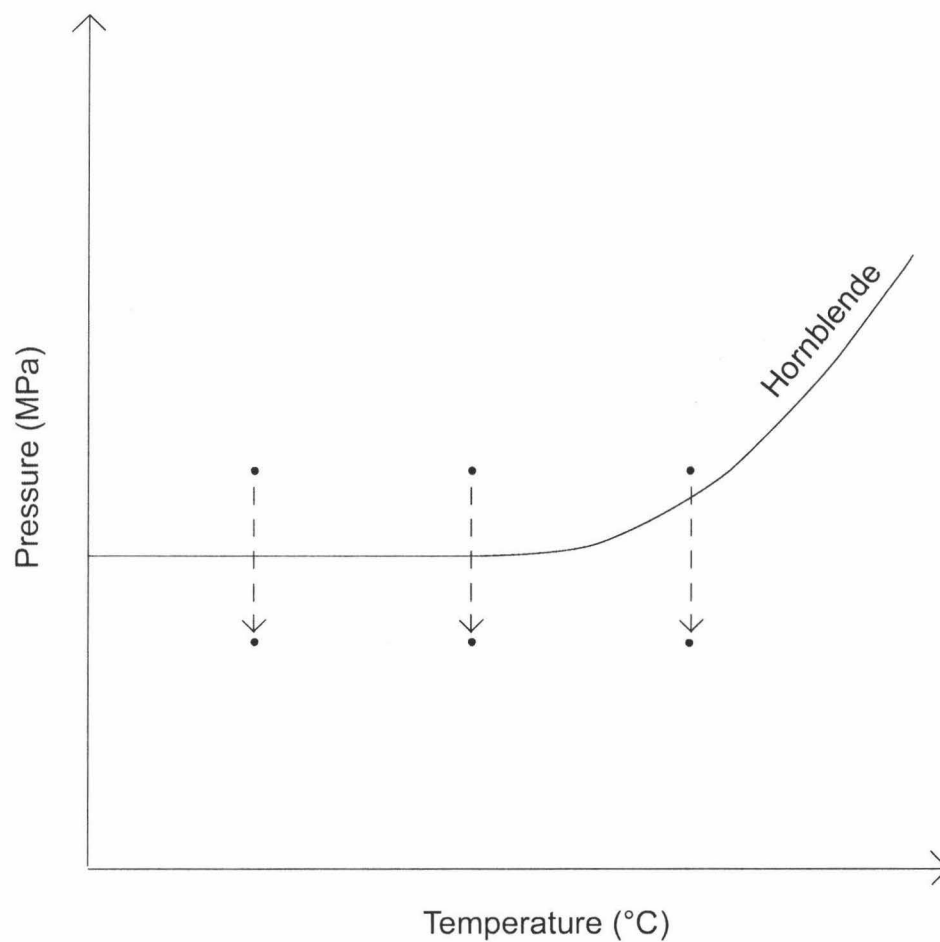
Figure 3 The schematic phase equilibria diagram is shown above. The three temperature values, 810, 850, and 890 °C, that were selected for the final condition after a single-step decompression. At 810 and 850 °C, it was assumed to have roughly the same distance from the hornblende stability field. Around 870 °C, the stability curve seems to start to bend regardless of sample.
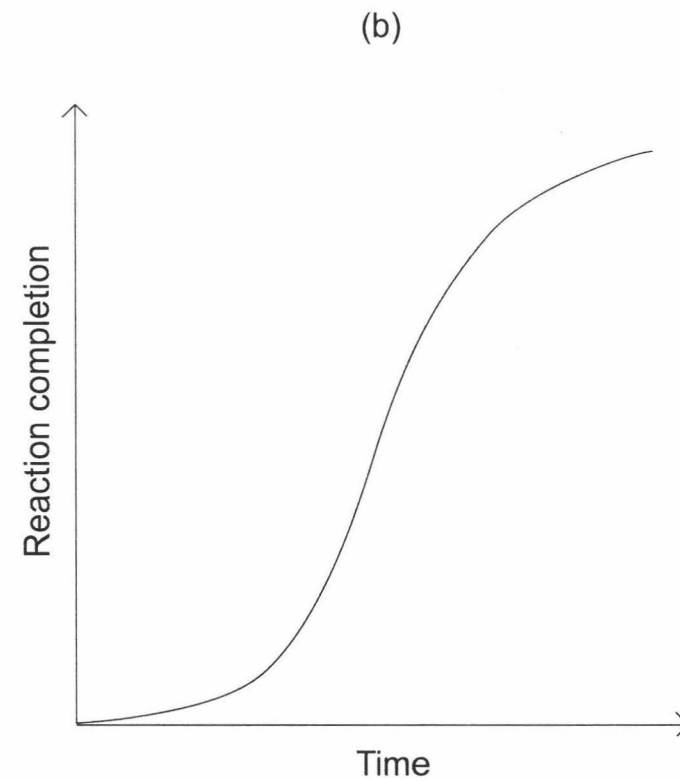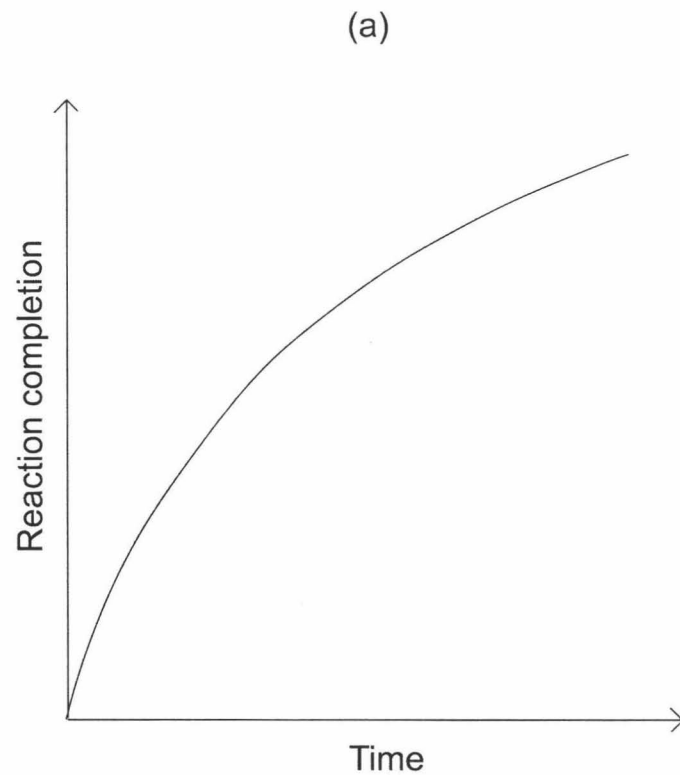
Figure 4 (a) A schematic diagram of completion fraction of the reaction vs. time for the parabolic rate law. The plot follows a deceleratory rate equation, in which diffusion is only rate limiting step of the reaction. **(b)** A schematic diagram of completion fraction of the reaction vs. time for the Avrami-Erofe'ev rate law. The plot follows a sigmoid rate equation (Avrami equation), in which nucleation and growth rates of the new rim minerals have control on the reaction rate in addition to the diffusion rate.
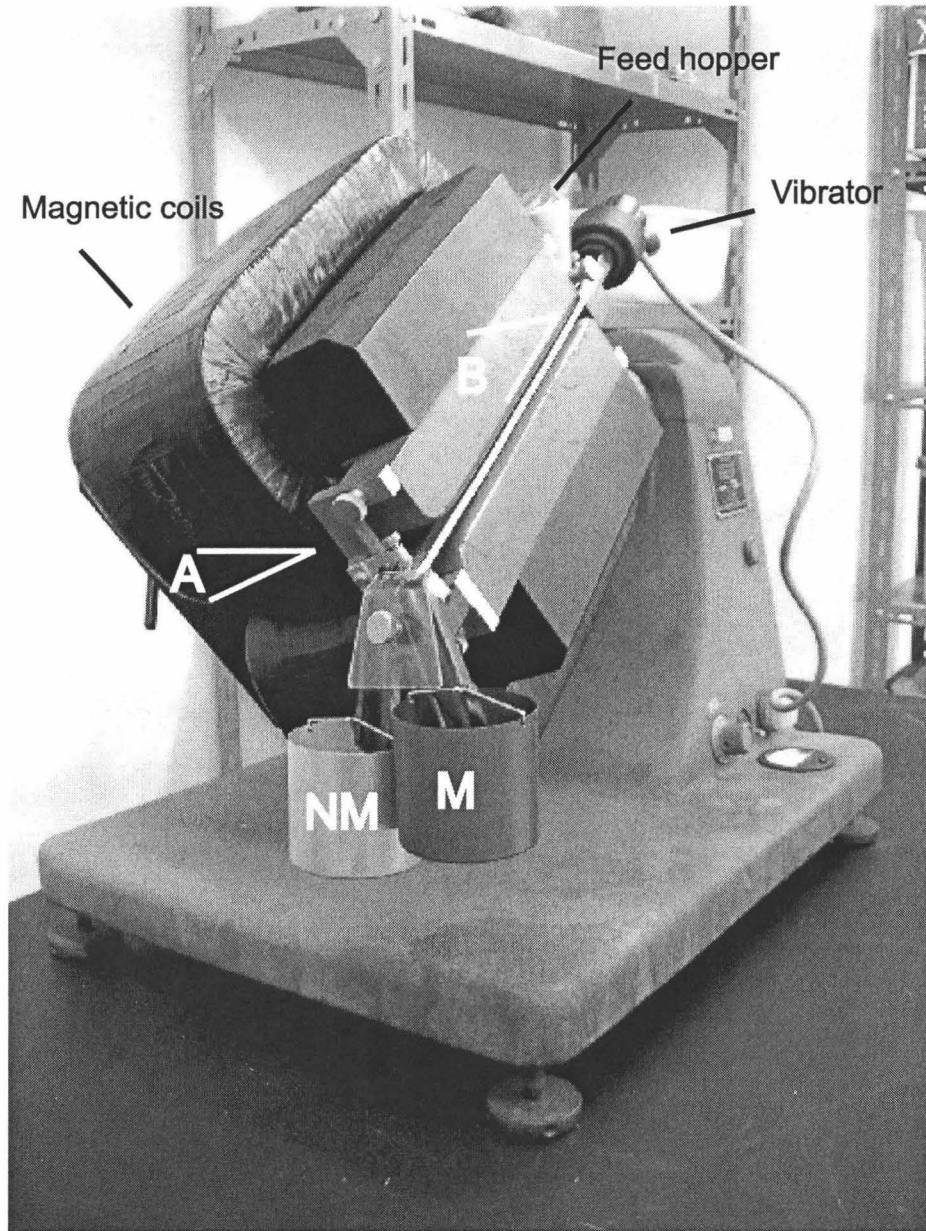
Figure 5 Frantz Isodynamic Separator Model L-1. Angle A is the slope angle of the separator perpendicular to the direction of sample path, which was set to 20°. Angle B is the slope angle parallel to the direction of sample path, which was set to 30°. Magnetic field was generated by magnetic coils, and vibration was generated by a vibrator. Particles are fed from a feed hopper at the top of 2 inclined chutes sloping toward 2 collection buckets. Vibration encourages particles out of the hopper and gravity causes the particles to slide down the chutes. A magnetic field applied by an electromagnet pulls magnetic particles into the upper inclined chute, and fall into a bucket M. In our case, those fell into this bucket was collected and called "hornblende concentrate", which was used to produce starting material for experimental runs.

Sheathed K-type thermocouple

Insulating cap

Starting material

Ag or Ag70Pd30 capsule welded at both ends

Clamshell type nichrome resistance furnace, mounted horizontally

Spacers

Ni filler rod

Ni alloy vessel (Waspaloy)

Heating coil

Pressurizing H2O

Cone-seat pressure seals

To line (pump, gauges, reservoir)
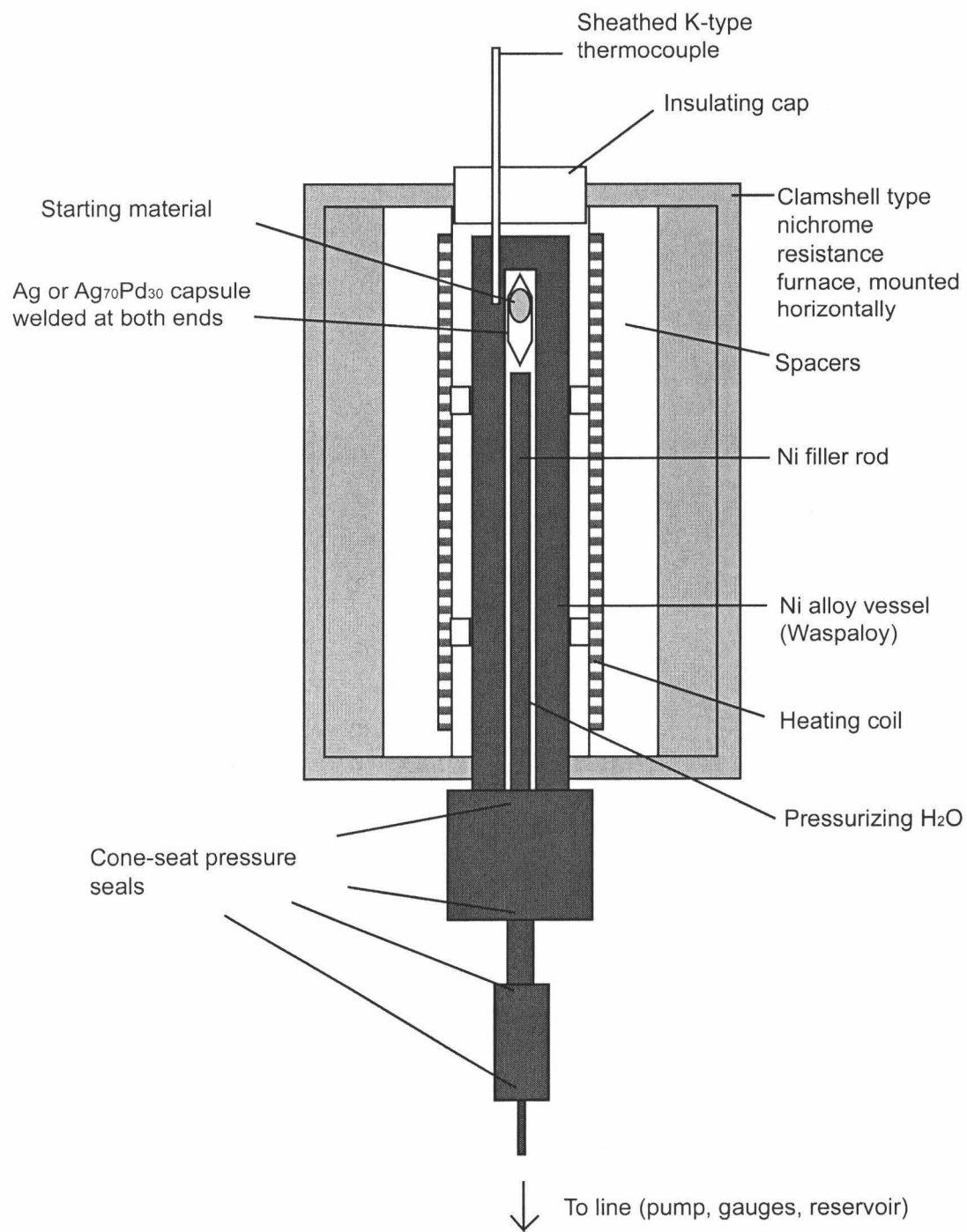
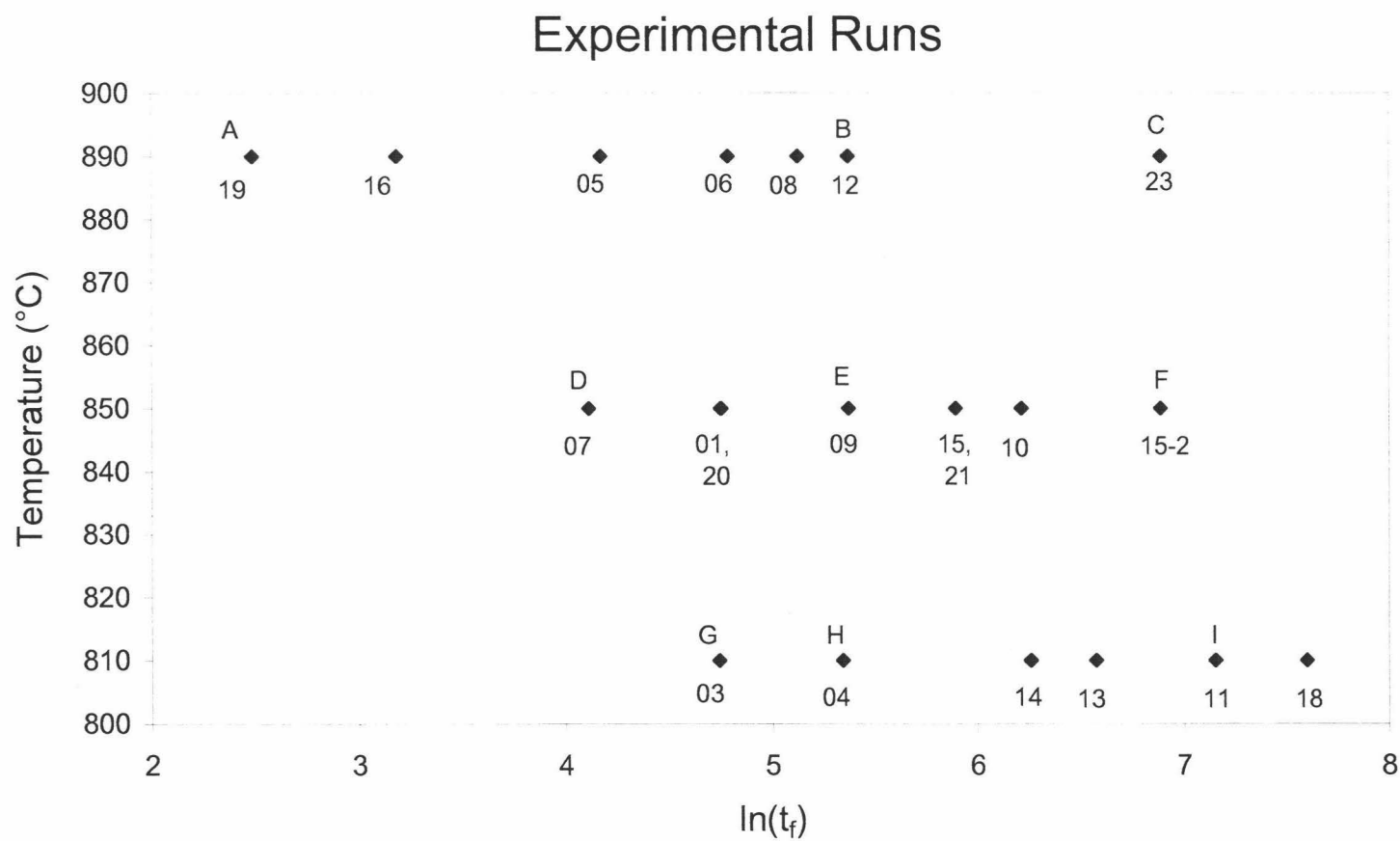**Figure 6** Top view of the furnace with experimental assembly inside.

Figure 7 A grid of experimental runs SHW-01, SHW-03, SHW-04, SHW-06, SHW-08 - SHW-23 (excluding failed and controlled experiments). X axis is natural logarithm of time (hours) at final conditions, and y axis is final temperature (°C). Letters A-H written above nine of points correspond to BSE images in Figure 11.
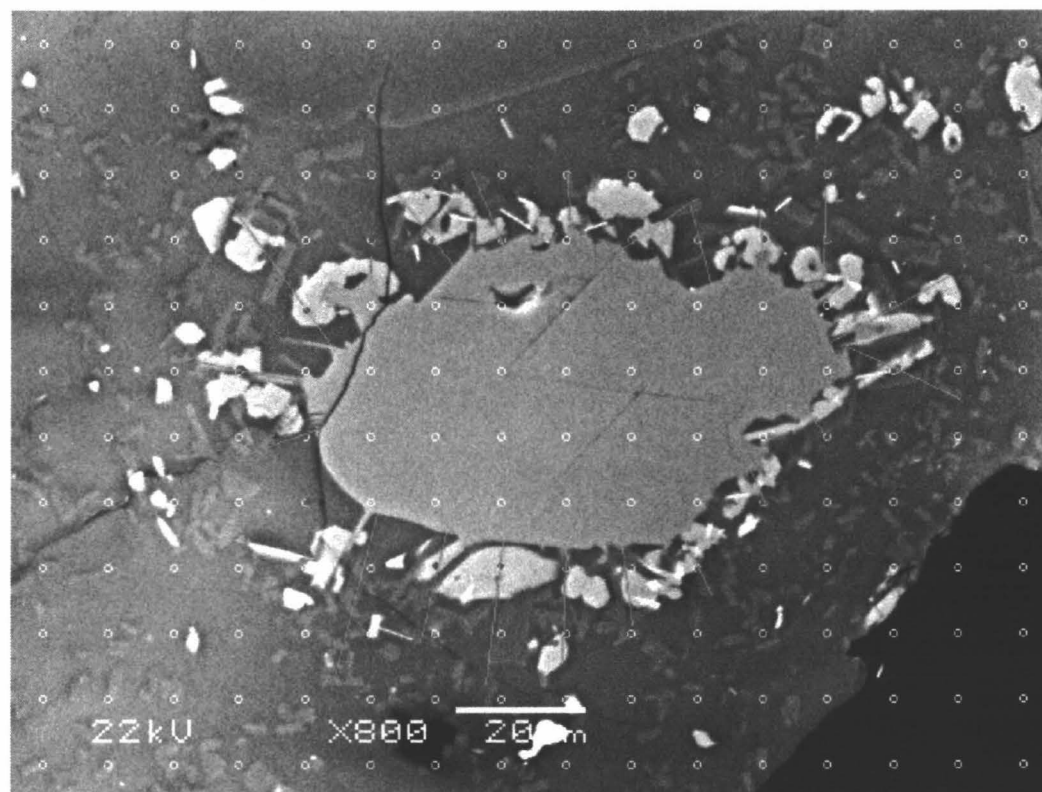
Figure 8 Image processing using a software ImageJ is shown. This is the BSE image of one of the hornblnede crystals in SHW-06. The scale in the image created by SEM was used to set the true scale. First, a 10 μm x 10 μm grid consists of small, white open circles was overlaid on the BSE image. Circles closest to the perimeter of the crystal was painted with pink dots. This is used to make certain the rim width is measured approximately every 10 μm at the hornblende perimeter. Then, blue lines perpendicular to the perimeter of the hornblende crystal were drawn from the perimeter of the hornblende to the furthermost edge of rim phases with intersecting the nearest pink dot. The length of the lines were calculated by ImageJ based on the scale and recorded.
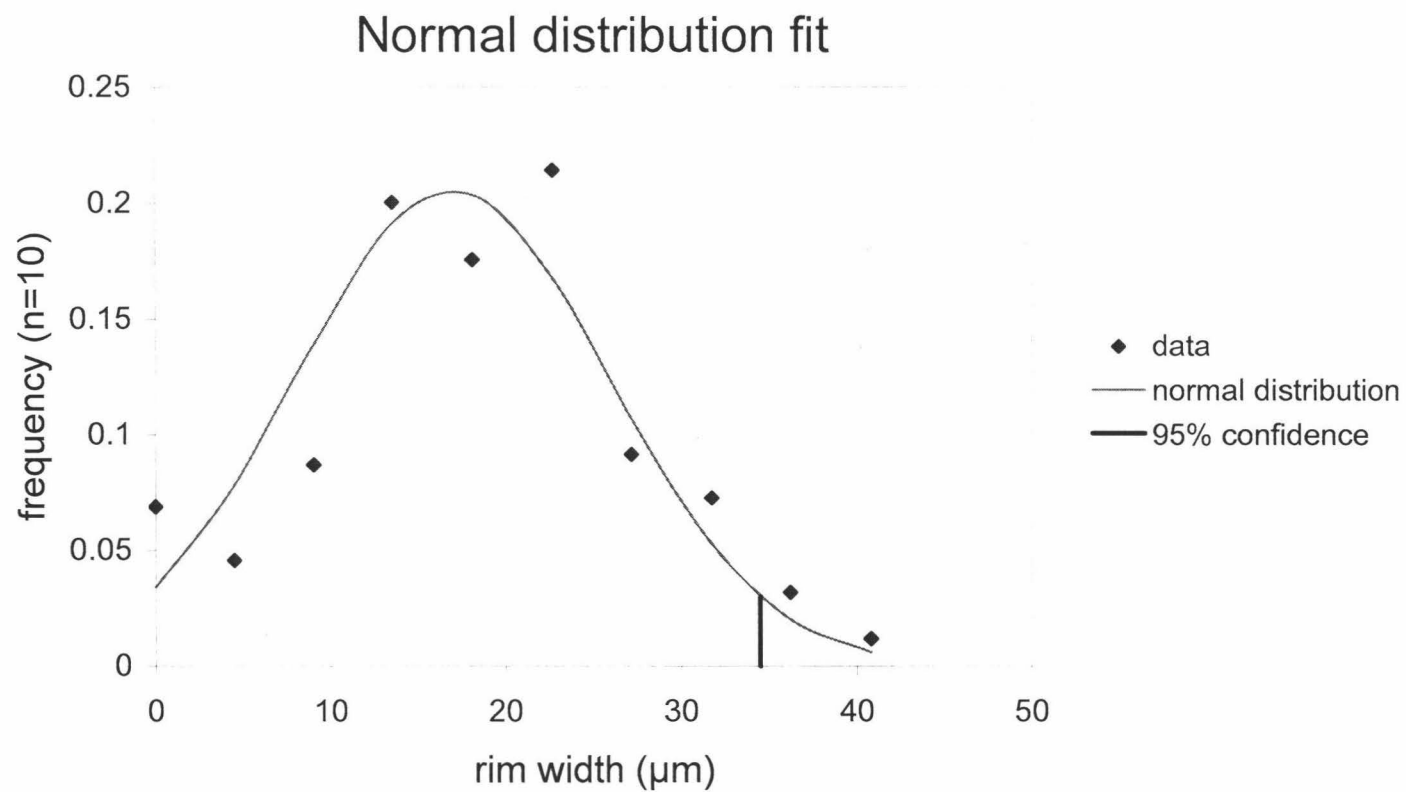
Figure 9 The frequency vs. mean rim width for 10 crystals (shown as n = 10) in SHW-06 and a theoretical normal distribution curve for this sample are shown as an example of this process. The 95 % confidence boundary shows the upper boundary below which 95 % of the measurements will lie theoretically.
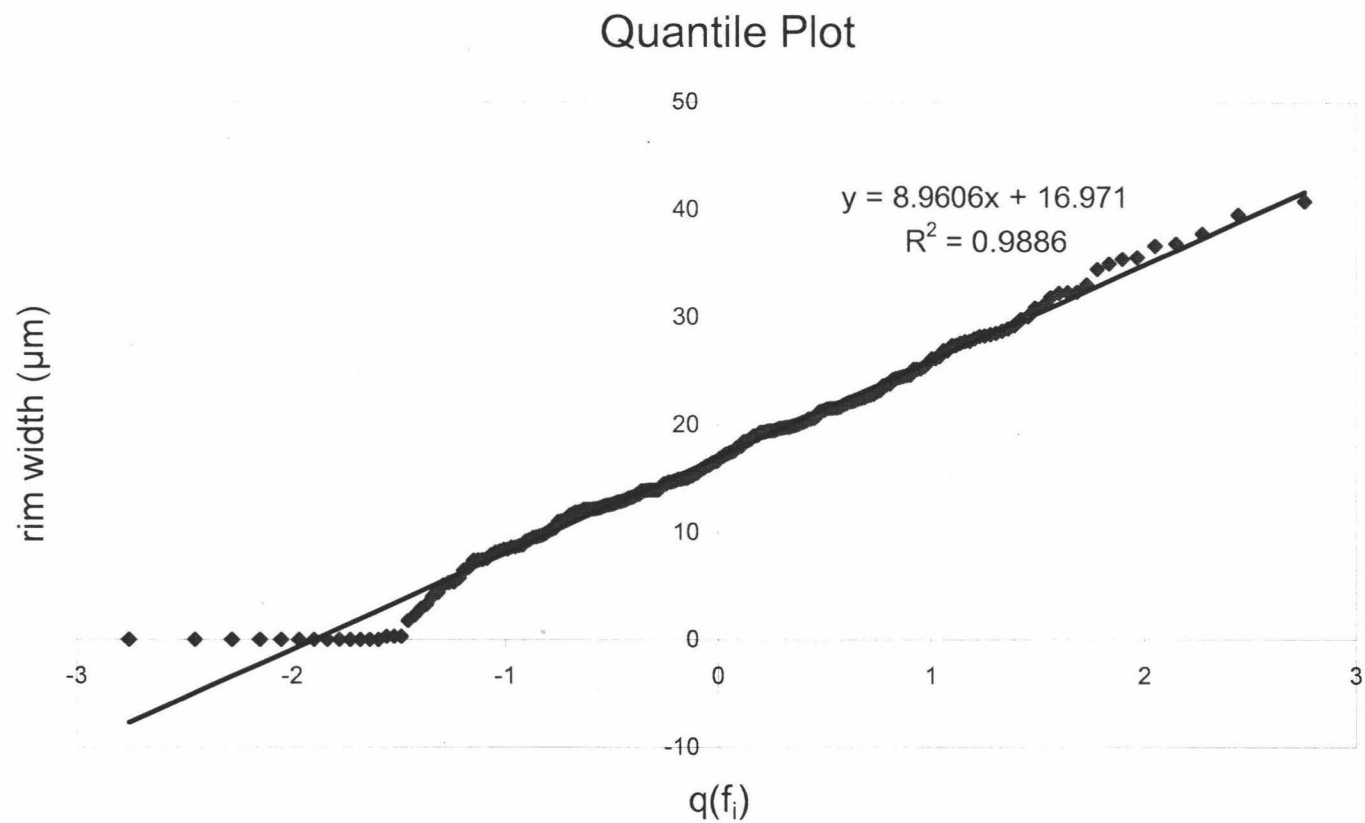
Figure 10 An example of quantile plot, rim width vs. quantile for SHW-06, generated by the method in Kirkup (2002). The values q(f_i) were calculated by the equation $4.91[f_i{\wedge}0.14 -(1-f_i){\wedge}0.14]$, where f_i is $(i-3/8)/(n+1/4)$. i is the arbitrary number assigned to each datum, and n is the total number of the values in the sample.
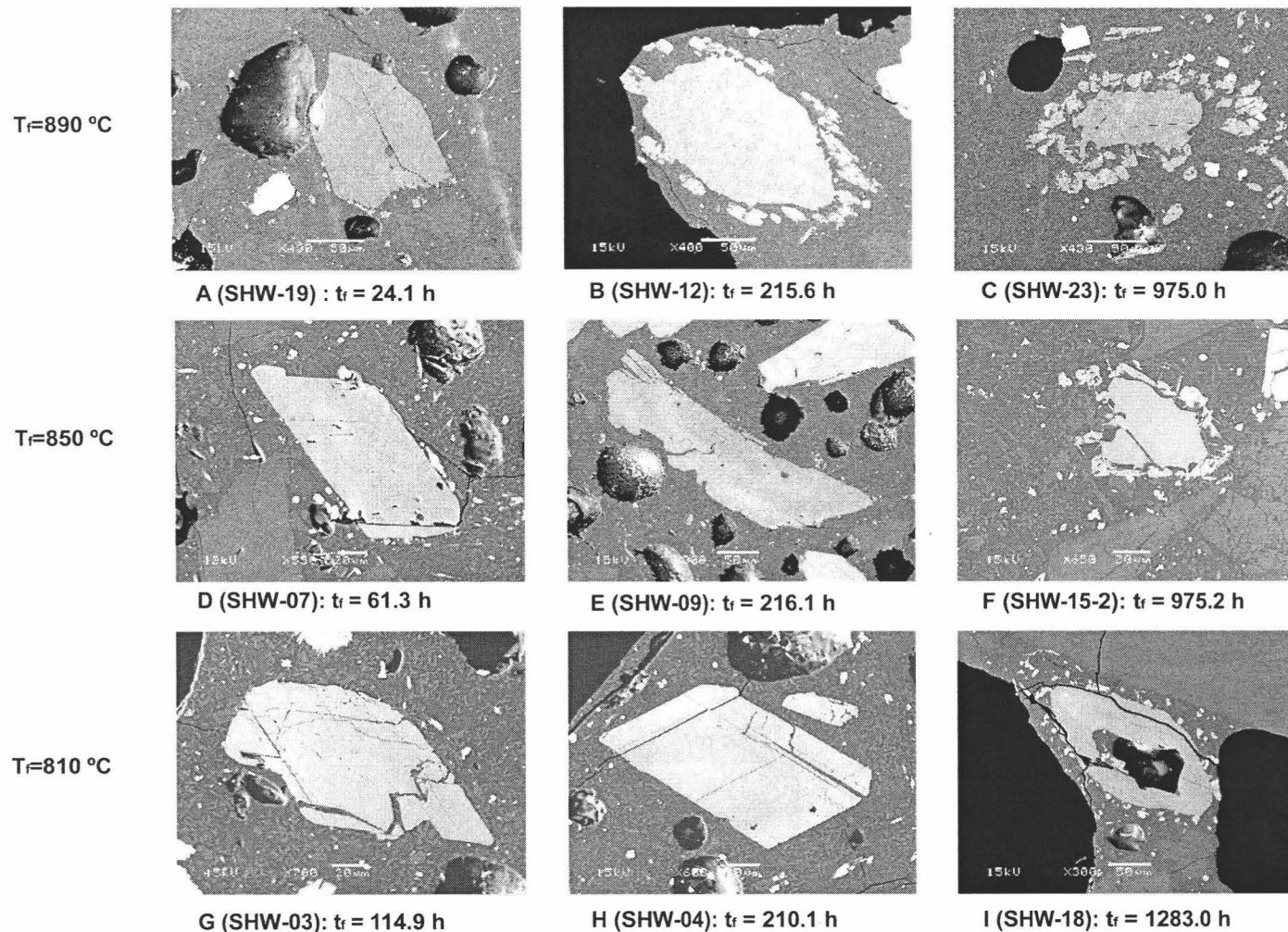
Figure 11 BSE images of hornblende crystals of 9 different experimental runs. The time at final conditions increases from left to right. The letters A-H below the images correspond to those in Figure 7. Time at final conditions are shown next to the letters. Crystals in A, B, C, F, and I show reaction rim growth but the rest appears to have no rim. Changes in the morphology of hornblende and rim crystals with time are fairly consistent at all temperatures. Crystals B, E, and H have approximately the same durations, but show different degree of reaction. Similarly, crystals C and F have approximately the same duration but have distinct rim widths.
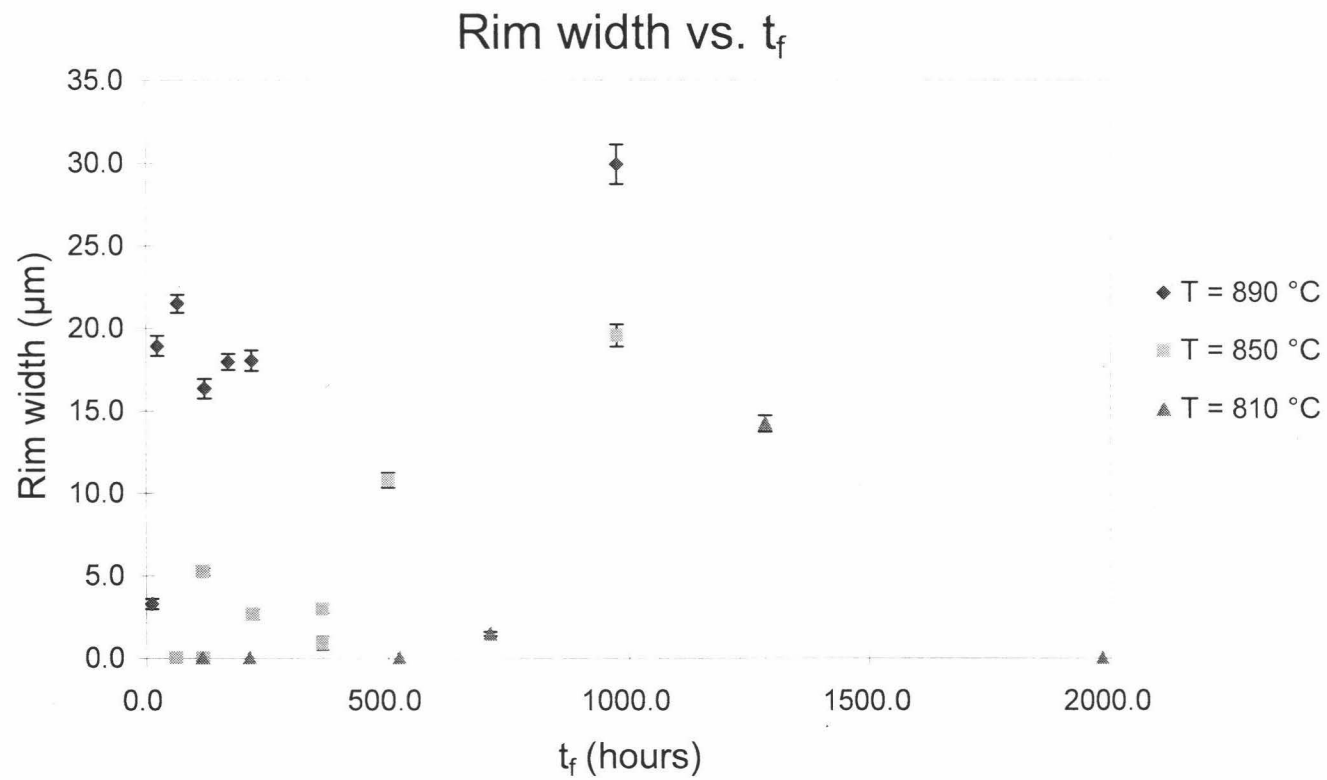
Figure 12 A plot of rim width vs. time at final conditions is shown. Error bars were calculated by the equation $\sigma/\sqrt{n}$, wehre σ is standard deviation of rim width and n is the number of measurements within each run. This method yields the error bars to indicate the accuracy of measurements.
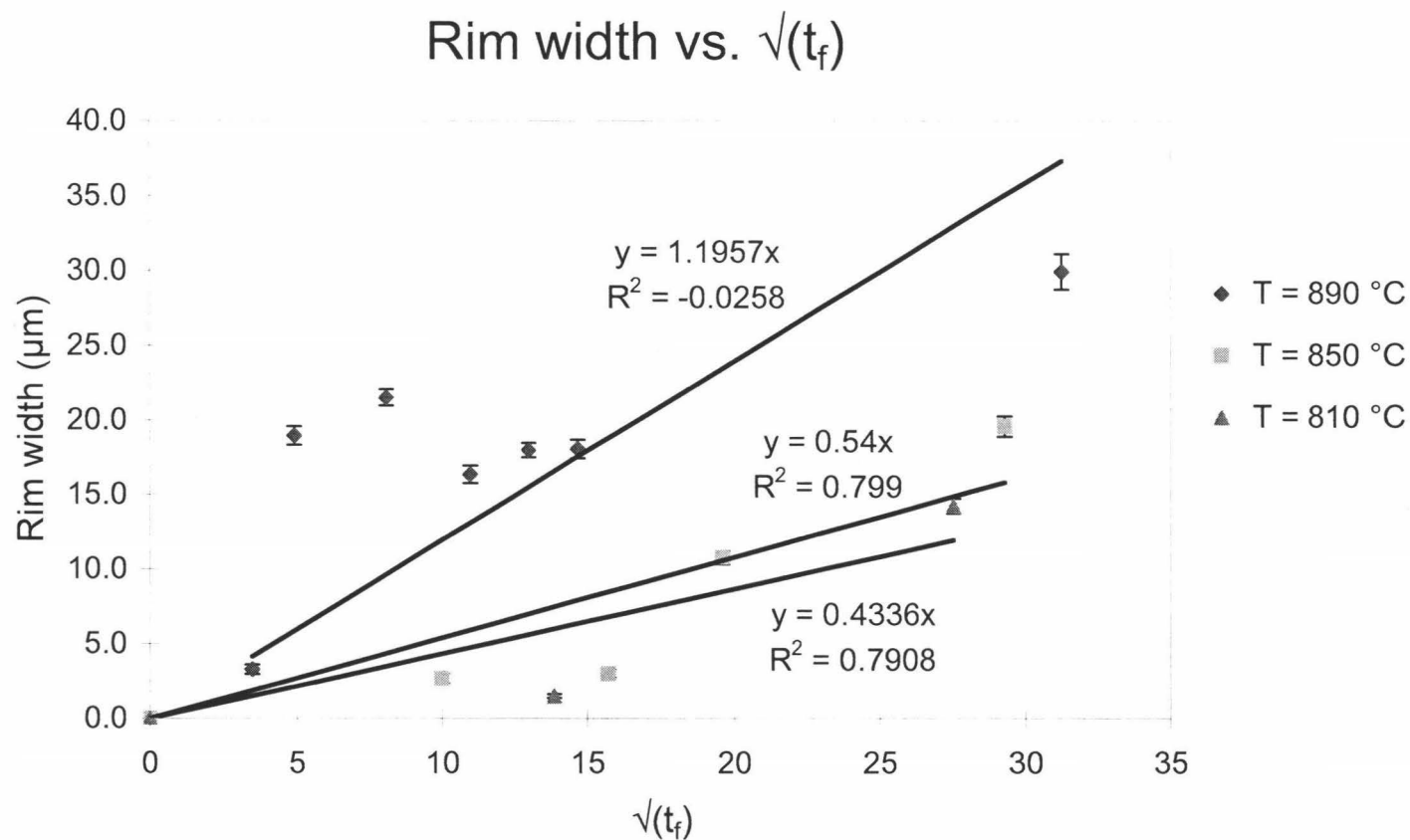
Figure 13 A plot of rim width vs. $\sqrt{(t_f)}$, where t_f is time at final conditions (hours). If there were multiple runs with no rim at the same temperature, only one of them with the longest duration was included in the plot and used to obtain the regression. Such data points were assumed to be at time zero. Therefore, in such cases, all data points at the same temperature were shifted toward the origin by square root of the true duration (hr) of the data points at zero. The data points for SHW-01 and 15 were replaced by the replicate runs SHW-20 and 21 (both at 850 °C) because those resutls seemed more realistic. The data point for SHW-18 was excluded from the plot.
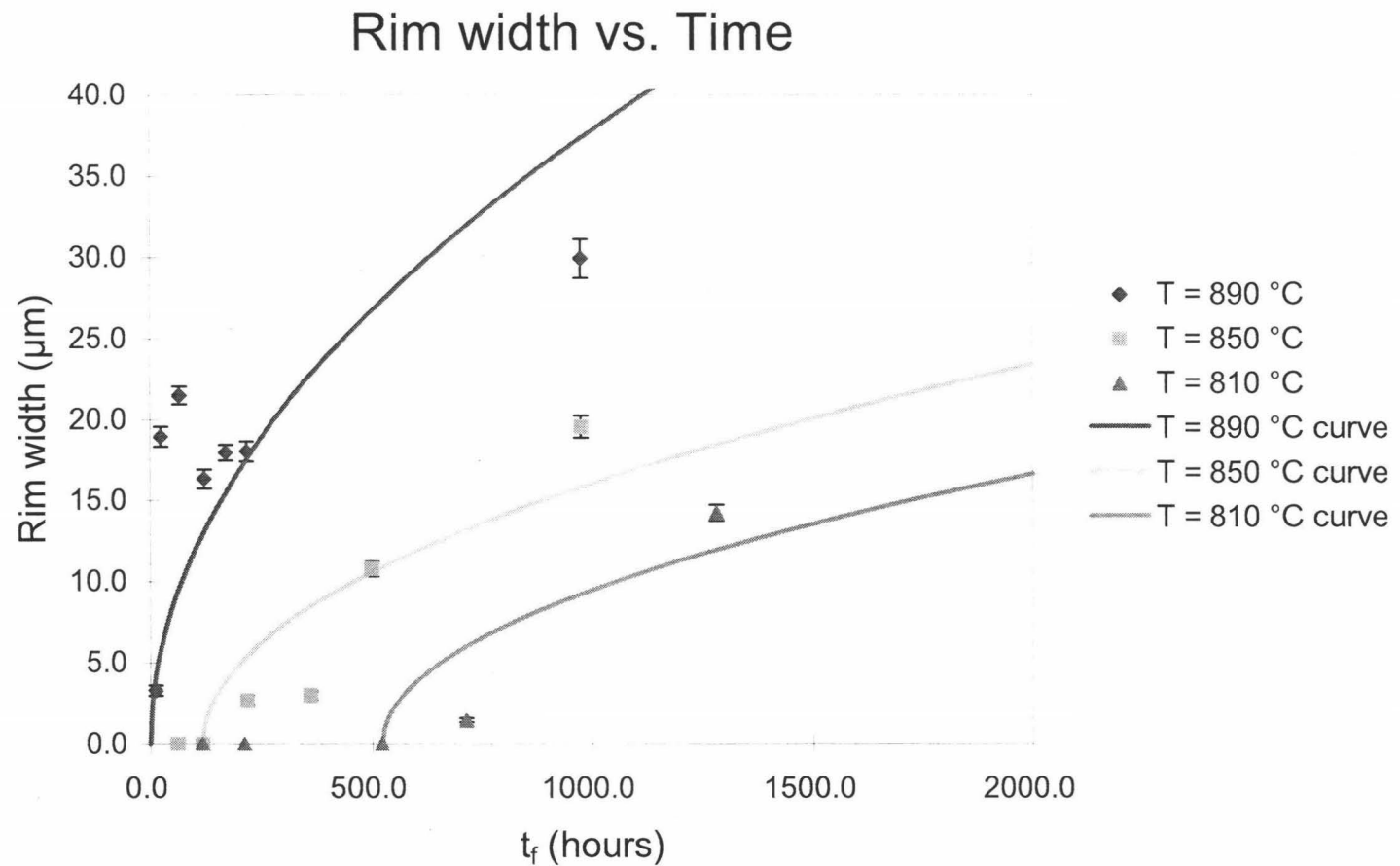
Figure 14 A plot of rim width vs. time at final conditions. Curves were obtained using one zero rim data point for each temperature as described in the caption of Figure 13. Slopes obtained from the linear regressions in Figure 13 were used to produce parabolic curves. The curves were shifted toward positive x direction by the duration of the first data points with zero rim. For 890 °C, it was assumed that the rim appeared as soon as the decompression took place.
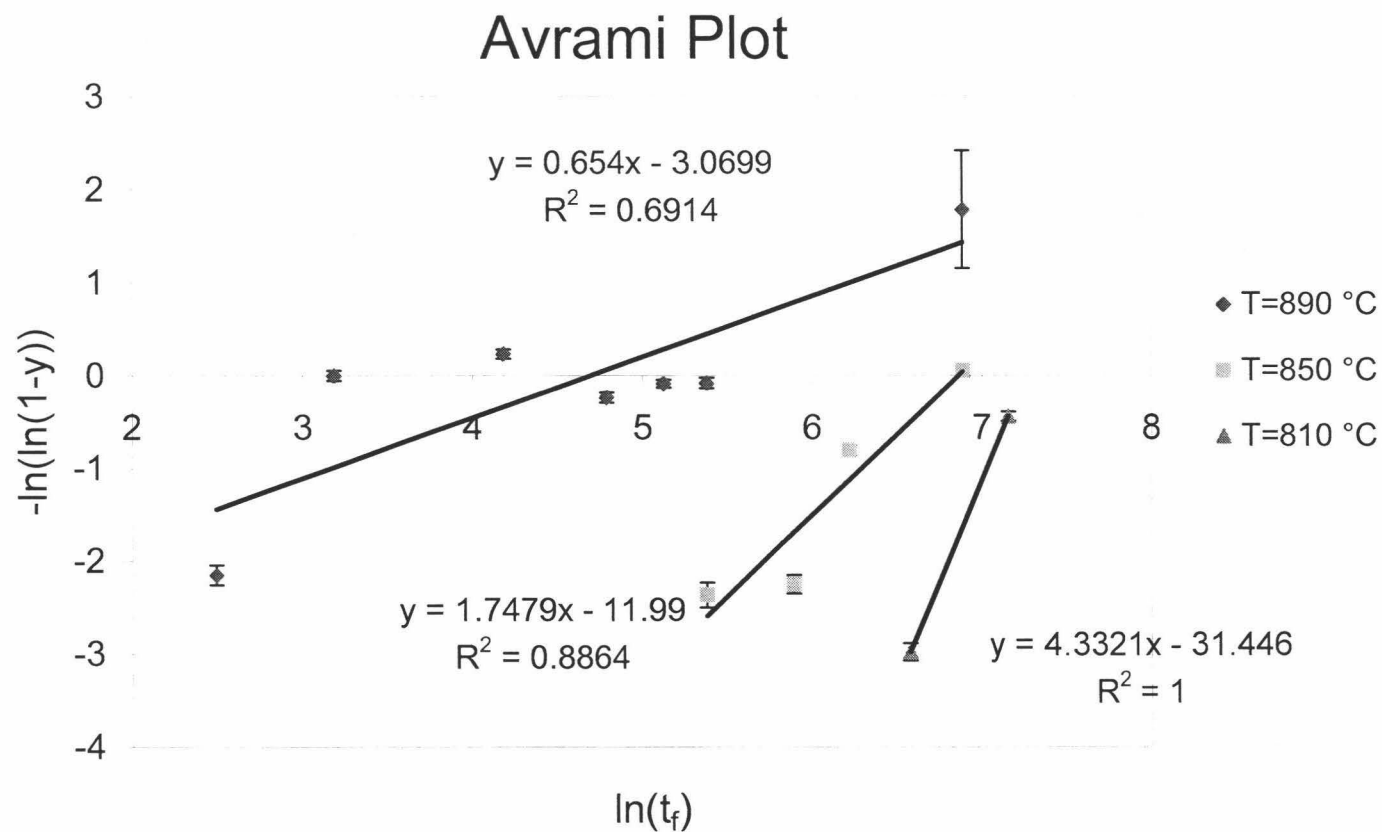
Figure 15 Avrami plot was produced by plotting -ln(ln(1-y)) against ln(tf), where y is completion fraction of rim growth assuming 30 μm is maximum width achieved at completion of the reaction, and t is the time at final conditions. All points with no rim were omitted because they cannot be plotted using logarithmic function. For 850 °C, the results for replicate runs replaced two previous runs as it is described in the caption of Figure 13. The regression for 810 °C is actually invalid because there are only two data points. This regression is disregarded in discussion.
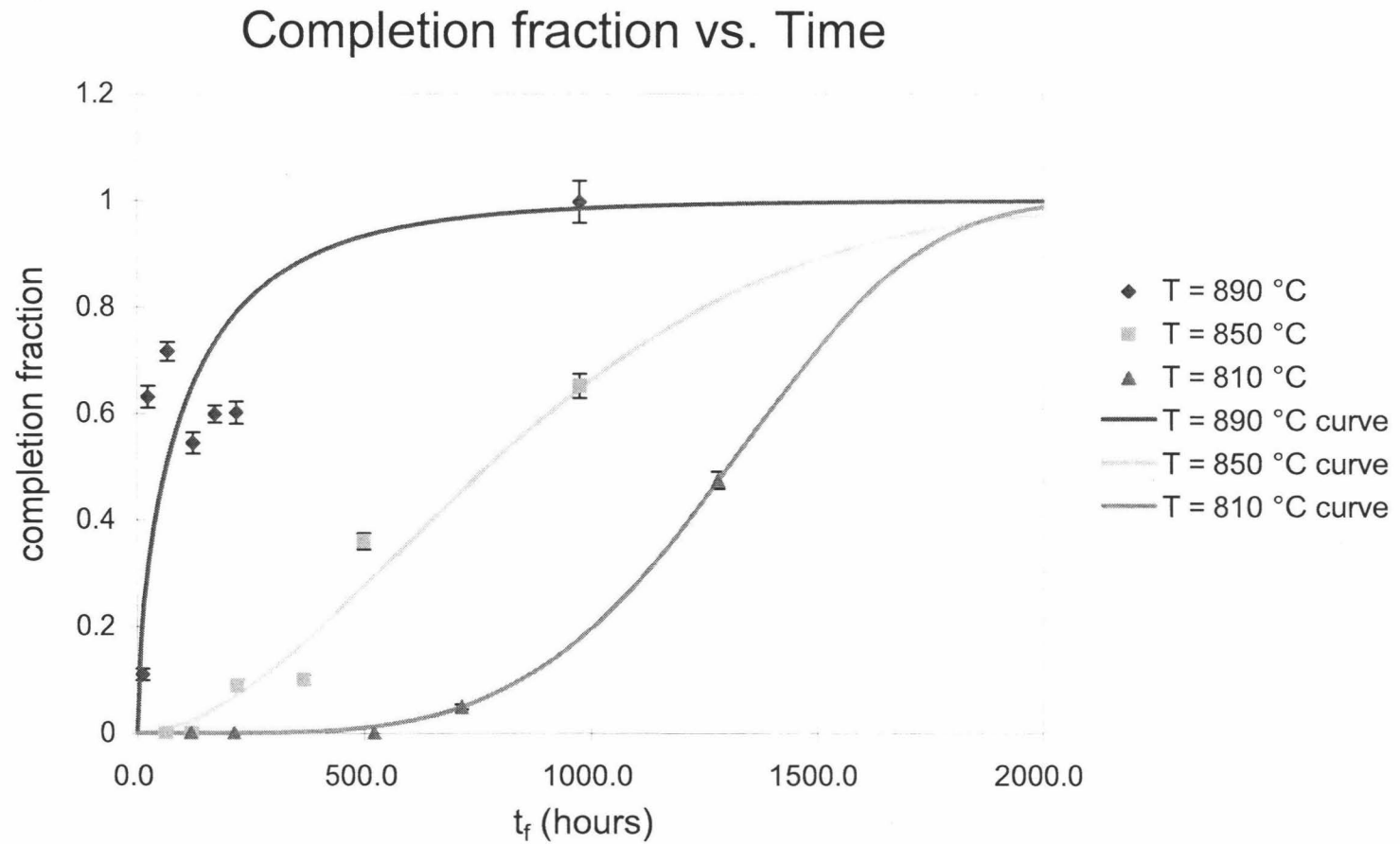
Figure 16 A plot of completion fraction of the breakdown reaction vs. time at final conditions. It was assumed that the maximum rim width is 30 μm at completion of the breakdown reaction based on the maximum rim width obtained in the experiments. Error bar values were obtained by deviding error bar values in the rim width vs. time plot (Figure 12) by assumed maximum rim width.
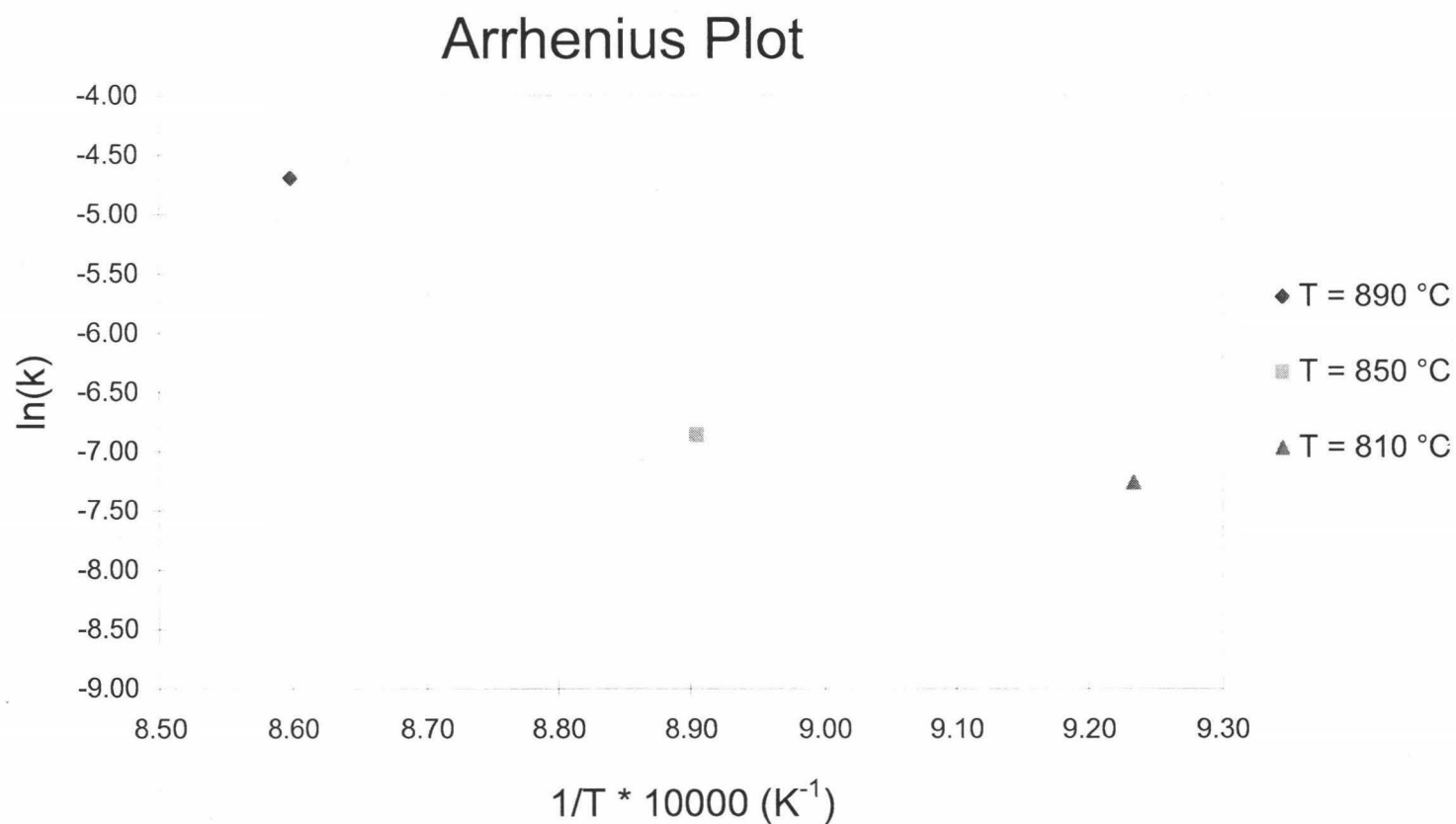
Figure 17 Arrhenius plot was generated by plotting $\ln(k)$ against $1/T$, where k is $\exp((\text{Y-intercept})/n)$ (Y-intercept is for Avrami plot and n is slope of Avrami plot), and T is temperature for final condition. The data point for 810 °C is actually invalid because the rate constant k was obtained from the Avrami plot linear regression line, which was obtained from only 2 data points for this temperature. This data point is disregarded in the discussion.

Table 1 **A.** Bulk compositions and temperatures of pumice of arc volcanoes. Mount St. Helen's data are from Gardner et al. (1995). The rest are from Browne and Gardner (2006). **B.** Glass compositions of the same pumice of arc volcanoes.

A

Volcano	Mt. St. Helens	Redoubt	Mt. St. Helens	Unzen	Soufriere Hills
Erupted event	Wn: 1480 ybp	12/15/1989	5/18/1980	Ave. comp. 5/91 to 5/95	Ave comp. 12/95 to 10/97
SiO2	67.2	63.4	63.8	65.2	60.0
Al2O3	16.5	17.7	17.5	15.9	17.9
TiO2	0.56	0.46	0.62	0.65	0.60
FeO*	3.72	4.68	3.73	4.44	6.57
MnO	0.08	0.13	0.07	0.10	0.18
CaO	3.77	5.8	4.81	5.01	7.57
MgO	1.22	1.77	2.04	2.49	2.72
K2O	1.62	1.68	1.26	2.42	0.82
Na2O	4.85	4.18	4.99	3.54	3.50
P2O5	-	0.19	0.14	0.16	0.14
Total	99.5	100.0	98.9	100.0	100.0
Temp. (°C)	850	~840	~880	~860	~840

B

Volcano	Mt. St. Helens	Redoubt	Mt. St. Helens	Unzen	Soufriere Hills
Erupted event	Wn: 1480 ybp	12/15/1989	5/18/1980	Ave. comp. 5/91 to 5/95	Ave comp. 12/95 to 10/97
SiO2	74.8	76.6	72.5	74.4	71.4
Al2O3	13.9	12.7	14.6	11.3	13.6
TiO2	0.21	0.24	0.36	0.37	0.28
FeO*	1.65	1.01	2.07	1.43	2.78
MnO	0.04	0.03	0.09	0.02	0.13
CaO	1.69	1.16	2.36	1.09	4.86
MgO	0.30	0.24	0.50	0.35	1.64
K2O	2.29	3.44	2.18	3.97	1.60
Na2O	5.17	3.93	5.16	2.77	3.73
P2O5	-	-	-	-	-
Total	100.1	99.4	99.8	95.7	100.0
Temp. (°C)	850	~840	~880	~860	~840

* FeO = total Fe

Table 2 A list of experiments and their conditions. All experiments are single-step decompression and starting material is SH-591-1 reconstituted powder (various grain sizes in the proper proportions) + ~10 wt.% hornblende concentrate. Precise notes on each experiment are listed in Appendix 1.

sample number	mass solids	mass H2O (after bake)	% H2O (H2O/solids)	t at initial conditions (h)	Pfinal (MPa)	Tfinal (°C)	t at final conditions (h)
SHW-03	0.0800	0.0108	13.5	25.5	65	810	114.9
SHW-04	0.1081	0.0118	10.9	24.0	65	810	210.1
SHW-14	0.0802	0.0109	13.5	36.3	65	810	522.1
SHW-13	0.0806	0.0108	13.4	36.3	65	810	714.1
SHW-11	0.0801	0.0098	12.3	48.2	65	810	1283.0
SHW-18	0.0807	0.0108	13.4	24.4	65	810	1982.2
SHW-02[a]	0.0808	0.0092	11.3	24.1	65	810	-
SHW-07	0.0809	0.0097	12.0	24.3	65	850	61.3
SHW-01	0.1181	0.0099	8.4	24.1	65	850	115.6
SHW-20[b]	0.0820	0.0098	11.9	24.1	65	850	116.0
SHW-09	0.0810	0.0107	13.2	24.6	65	850	216.1
SHW-15	0.0801	0.0108	13.5	36.8	65	850	362.3
SHW-21[b]	0.0810	0.0094	11.6	24.0	65	850	362.4
SHW-10	0.0809	0.0107	13.3	24.6	65	850	499.9
SHW-15-2	0.0801	0.0108	13.5	36.8	65	850	975.2
SHW-19	0.0812	0.0063	7.8	24.0	65	890	12.1
SHW-16	0.0806	0.0109	13.6	24.2	65	890	24.1
SHW-05	0.0818	0.0104	12.7	24.1	65	890	65.2
SHW-22[a]	0.0809	0.0082	10.2	24.3	65	890	-
SHW-06	0.0809	0.0064	8.0	24.1	65	890	120.1
SHW-08	0.0817	0.0084	10.2	24.6	65	890	168.1
SHW-12	0.0808	0.0082	10.1	35.7	65	890	215.6
SHW-23	0.0805	0.0070	8.7	24.2	65	890	975.0
SHW-17[c]	0.0805	0.0107	13.3	24.0	-	-	-

[a] failed runs

[b] replicate runs. SHW-19 replicated SHW-1, and SHW-21 replicated SHW-15.

[c] controlled run

Table 3 Textural description of hornblende and rim crystals for each experimental run. Failed runs and a controlled run were omitted. Approximate diameter range of rim pyroxene basal sections were obtained by measuring 5 smallest crystals and 5 largest crystals.

sample name	final T (°C)	t at final conditions (h)	rim width (μm)	Roundness of hornblende compared to controlled expmt SHW-17 (setting it as standard)	dispersion of rim crystals	approximate diameter range of rim pyroxene basal sections (μm)
SHW-03[a]	810	114.9	0.0	(no rim)	-	-
SHW-04[b]	810	210.1	0.0	(no rim)	-	-
SHW-14	810	522.1	0.0	(no rim)	-	-
SHW-13	810	714.1	1.5	standard	-	-
SHW-11	810	1283.0	14.2	slightly rounded	sparse	2.7 - 7.2
SHW-18	810	1982.2	0.0	(no rim)	-	-
SHW-07	850	61.3	0.0	(no rim)	-	-
SHW-01	850	115.6	5.2	slightly rounded-standard	-	1.3 - 3.8
SHW-20[a]	850	116.0	0.0	(no rim)	-	-
SHW-09[b]	850	216.1	2.7	rounded-standard	-	1.6 - 5.9
SHW-15	850	362.3	0.9	rounded	-	-
SHW-21	850	362.4	3.0	standard	sparse	0.5 - 4.0
SHW-10	850	499.9	10.8	rounded	packed	1.3 - 9.0
SHW-15-2	850	975.2	19.6	very rounded	packed	1.4 - 10.4
SHW-19	890	12.1	3.3	standard	sparse	0.9 - 5.1
SHW-16	890	24.1	18.9	slightly rounded	sparse	0.7 - 5.4
SHW-05	890	65.2	21.5	slightly rounded	sparse	1.5 - 8.5
SHW-06[a]	890	120.1	16.3	slightly rounded (various)	packed	1.0 - 9.4
SHW-08	890	168.1	18.0	rounded	packed	1.3 - 7.2
SHW-12[b]	890	215.6	18.0	very rounded	packed	1.1 - 8.3
SHW-23	890	975.0	29.9	irregular	packed	1.2 - 14.4

[a] The runs at similar durations (114.9 - 120.1 hours)
[b] The runs at similar durations (210.1-216.1 hours)

Table 4 Mean rim width of each crystal, mean rim width of each experimental run, standard deviation of all measurements for each run, total measurements for each run, and error bar values derived from standard deviation and the number of total measurements are listed. A total of 3-16 crystals were used to obtain rim thickness for each experimental run. Thickness was measured roughly every 10 μm on hornblende perimeter. Normal distribution curves were generated for samples SHW-06, 11, 12, and 15-2 using standard deviation and error values listed below (e.g., Figure 9). The error values derived from the equation σ/sqrt(n) describe accuracy of measurement rather than range of distribution.

sample name	SHW-01	SHW-03	SHW-04	SHW-05	SHW-06	SHW-07	SHW-08	SHW-09	SHW-10	SHW-11	SHW-12
crystal #											
1	3.3	-	-	13.6	16.0	-	19.7	1.9	10.0	15.0	17.0
2	4.6	-	-	15.0	8.8	-	16.6	1.0	15.4	11.0	16.0
3	4.4	-	-	23.5	18.1	-	22.0	7.0	12.8	23.1	23.6
4	2.1	-	-	25.5	18.2	-	20.8	1.0	13.4	15.3	17.8
5	3.7	-	-	23.3	13.0	-	18.0	1.1	7.6	10.0	14.2
6	4.9	-	-	23.4	18.3	-	14.9	1.0	8.0	15.6	18.8
7	6.6	-	-	13.4	13.9	-	17.4	3.9	10.5	19.5	14.7
8	5.3	-	-	20.8	22.1	-	19.0	0.6	12.3	6.0	22.2
9	8.1	-	-	24.0	18.5	-	17.6	7.2	7.9	11.7	19.7
10	7.9	-	-	18.2	-	-	13.7	2.1	9.9	15.0	16.5
11	6.6	-	-	30.6	-	-	-	-	-	-	-
12	5.4	-	-	42.1	-	-	-	-	-	-	-
13	-	-	-	23.5	-	-	-	-	-	-	-
14	-	-	-	16.1	-	-	-	-	-	-	-
15	-	-	-	17.1	-	-	-	-	-	-	-
16	-	-	-	13.7	-	-	-	-	-	-	-
mean	5.2	-	-	21.5	16.3	-	18.0	2.7	10.8	14.2	18.0
standard deviation (σ)	4.8	-	-	12.2	9.0	-	9.8	6.4	8.8	10.2	11.0
total measurements (n)	465	-	-	495	227	-	421	388	373	424	316
error bar values σ/√(n)	0.22	-	-	0.55	0.59	-	0.48	0.32	0.46	0.50	0.62

sample name	SHW-13	SHW-14	SHW-15	SHW-15-2	SHW-16	SHW-17	SHW-18	SHW-19	SHW-20	SHW-21	SHW-22	SHW-23
crystal #												
1	2.2	-	3.4	13.6	21.5	-	-	2.5	-	1.2	-	30.4
2	1.3	-	2.6	17.2	19.9	-	-	1.2	-	2.6	-	33.0
3	2.0	-	0.7	23.3	27.6	-	-	3.6	-	1.9	-	26.4
4	2.6	-	0.7	21.5	25.4	-	-	2.9	-	9.6	-	-
5	1.5	-	0.1	20.0	14.3	-	-	4.1	-	3.1	-	-
6	1.1	-	0.1	26.6	16.5	-	-	2.1	-	1.1	-	-
7	1.0	-	0.2	16.5	18.4	-	-	4.4	-	2.9	-	-
8	0.9	-	0.6	15.0	14.7	-	-	2.9	-	3.0	-	-
9	1.6	-	0.5	20.5	16.3	-	-	8.9	-	1.5	-	-
10	0.8	-	0.4	21.5	14.8	-	-	0.0	-	2.9	-	-
11	-	-	-	-	-	-	-	-	-	-	-	-
12	-	-	-	-	-	-	-	-	-	-	-	-
13	-	-	-	-	-	-	-	-	-	-	-	-
14	-	-	-	-	-	-	-	-	-	-	-	-
15	-	-	-	-	-	-	-	-	-	-	-	-
16	-	-	-	-	-	-	-	-	-	-	-	-
mean	1.5	-	0.9	19.6	18.9	-	-	3.3	-	3.0	-	29.9
standard deviation (σ)	2.3	-	7.3	9.3	10.9	-	-	5.7	-	5.3	-	10.6
total measurements (n)	317	-	352	183	311	-	-	320	-	379	-	79
error bar values σ/√(n)	0.13	-	0.39	0.68	0.62	-	-	0.32	-	0.27	-	1.19

Appendix 1 Notes on the experimental runs and quenching. Samples are in the same order as in Table 2.

sample number	Notes
SHW-03	No problem was observed.
SHW-04	No problem was observed.
SHW-14	Pressure in the vessel was not maintained. Pressure-check right before decompression showed pressure decrease by 2.7 MPa. Decided to quench and reuse the charge.
SHW-13	No problem was observed.
SHW-11	No problem was observed.
SHW-18	The power outage due to earthquakes on 10-14-06 @~7:00am. The run was re-started from the final condition. Recrystallization of Ni took place at the filler rod and inside the vessel.
SHW-02[a]	We discovered that the water line was clogged and had no control over the pressure. The experiment failed.
SHW-07	No problem was observed.
SHW-01	No problem was observed.
SHW-20[b]	It was quenched while the pressure was maintained at 57-68 MPa.
SHW-09	No problem was observed.
SHW-15	No problem was observed.
SHW-21[b]	Starting time was arbitrary (convenient for us), before we closed the valve. Upon quenching, the temperature dropped to as low as 847 °C when tried to use thermocouple holder. However, it was quenched immediately, so there was probably no effect on the run. The pressure was maintained at 55-75 MPa.
SHW-10	The pressure decreased by 20 MPa in <24 h after closing the valve. Therefore, the initial condition was repeated for extra 24 h. The leaking continued and the vavle was opend to the line with the reservoir open at 70 MPa from 07-06-06) until 1:23 pm 07-21-06 when it was quenched prior to the scheduled power outage. During temporary quenching, P was maintained at 65-75 MPa. The connection to the vessel was swiched to another one in order to aviod any possible risk for leaking, and no more leaking was observed. It was quenched again at 7:50 am 8-18-06 prior to another scheduled power outage (pressure maintained at ~44-65 MPa). It was put up at final condition at 3:03 pm 8-18-06. A pressure drop by 4 MPa was ovserved during pressure check at 1:49 pm 8-19-06. The pressure was normal on 8-20-06.
SHW-15-2	A portion of SHW-15 was separated and used as a starting material for this run.
SHW-19	It was quenched while the pressure was maintained at 56-63 MPa.
SHW-16	It was quenched at 1:13 pm 07-21-06 prior to the scheduled power outage. During the temporary quenching, the pressure was maintained at 65-80 MPa.
SHW-05[a]	A possible leaking from the valve was recognized. The pressure dropped by 0.35-0.4 MPa after starting the experiment. Leaking was not observed later, therefore, probably the drop was within an error. It was quenched at 1:07 pm 07-21-06 prior to the shceduled power outage. During the temporary quenching, the pressure was maintained at 65-80 MPa.
SHW-05	It was quenched at 1:18 pm 07-21-06 prior to the scheduled power outage. During the temporary quenching, the pressure was maintained at 62-65 MPa.
SHW-22[a]	Thermocouple failure during weekend (12-02-06 - 12-03-06). The experiment failed.
SHW-06	No problem was observed.
SHW-08	The pressure increse by 0.75 MPa was observed at a pressure check at 2:20 pm 8-1-06.
SHW-12	No problem was observed.
SHW-23	No problem was observed.
SHW-17[c]	No problem was observed.

[a] failed runs

[b] repeated runs. SHW-19 replicated SHW-1, and SHW-21 replicated SHW-15.

[c] controlled run